arXiv:1611.06832v1 [physics.flu-dyn] 21 Nov 2016

Stochastic modelling and diffusion modes for POD models and small-scale flow analysis

Valentin Resseguier[1,2]*, Etienne Mémin[1],
Dominique Heitz[3,1] and Bertrand Chapron[2]
[1]Fluminance, Inria/Irstea/IRMAR,
Campus de Beaulieu, 35042 Rennes, France
[2]LOPS, Ifremer, Pointe du Diable, 29280 Plouzané, France
[3]Irstea, UR OPAALE, F-35044 Rennes, France

November 22, 2016

ABSTRACT

We introduce a stochastic modelling in the constitution of fluid flow reduced-order models. This framework introduces a spatially inhomogeneous random field to represent the unresolved small-scale velocity component. Such a decomposition of the velocity in terms of a smooth large-scale velocity component and a rough, highly oscillating, component gives rise, without any supplementary assumption, to a large-scale flow dynamics that includes a modified advection term together with an inhomogeneous diffusion term. Both of those terms, related respectively to *turbophoresis* and *mixing* effects, depend on the variance of the unresolved small-scale velocity component. They bring to the reduced system an explicit subgrid term enabling to take into account the action of the truncated modes. Besides, a decomposition of the variance tensor in terms of *diffusion modes* provides a meaningful statistical representation of the stationary or nonstationary structuration of the small-scale velocity and of its action on the resolved modes. This supplies a useful tool for turbulent fluid flows data analysis. We apply this methodology to circular cylinder wake flow at Reynolds numbers $Re = 300$ and $Re = 3900$, respectively. The finite dimensional models of the wake flows reveal the energy and the anisotropy distributions of the small-scale diffusion modes. These distributions identify critical regions where corrective advection effects as well as structured energy dissipation effects take place. In providing rigorously derived subgrid terms, the proposed approach yields accurate and robust temporal reconstruction of the low-dimensional models.

1 Introduction

Surrogate empirical models of flow dynamics with a reduced set of degrees of freedom are widely used in fluid mechanics for control applications or physical analysis (Noack *et al.*, 2010). Within such modelling a few numbers of modes extracted from experimental or numerical measurements are used to represent the main dynamical behaviour of a flow. The modes in themselves may help unveiling recurrent dynamical patterns. Spectral approaches are quite natural for that purpose. Fourier representation has been used

*Email address for correspondence: valentin.resseguier@inria.fr

for a long time to characterize hydrodynamics instabilities. Proper Orthogonal Decomposition (POD) and the spectral representation of the velocity auto-correlation matrix is used to extract descriptive empirical spatial or temporal basis of the flow (Aubry *et al.*, 1988; Holmes *et al.*, 1996; Sirovich, 1987). More recently the Dynamic Modes Decomposition (DMD) relying on the eigenvectors of the Koopman operator (Koopman, 1931) and Takens delay embedding theorem (Takens, 1981) has been proposed to represent, from the evolution of observations, the principal modes of the dynamical system's attractor (Mezic, 2005; Rowley *et al.*, 2009; Schmid, 2010). Combination of both representations can be used as well to provide a suitable energy spectrum representation (Cammilleri *et al.*, 2013). In all those modal representations the construction of the reduced-order dynamics requires a truncation operation in which the most "influential" modes – with respect to a given criterion – are kept to describe the flow. In general, the action of the discarded modes must be modeled to get accurate and stable dynamical systems. The effect of those neglected processes encompasses dissipation effects but are also responsible of some energy redistribution and backscattering (Piomelli *et al.*, 1991).

In most of the flow low-order dynamics, the unresolved small-scale processes are represented on the basis of an eddy viscosity assumption (Boussinesq, 1877). This takes the form of a damping term in the reduced-order dynamical system. In Galerkin POD reduced models, this extra dissipation, which adds up to the linear molecular diffusion, is modeled by a constant coefficient (Aubry *et al.*, 1988) or through a modal constant vector (Cazemier *et al.*, 1998; Rempfer & Fasel, 1994). Recently, nonlinear functions have been proposed for a bluff body wake flow (Östh *et al.*, 2014). Although those models have demonstrated their efficiency in numerous situations, the estimation of the associated parameters and/or the choice of the nonlinear dependency between the eddy-viscosity coefficients and the modal coefficients constitute a sensible issue. Furthermore, from a physical interpretation point of view, the action of the small-scale velocity component is interpreted only with regard to an homogeneous stationary dissipation effect. Neither preferential local direction of diffusion related to the flow physics is considered, nor energy redistribution action by the small scales.

Robust techniques based on optimal control strategies have also been proposed for building reduced dynamical models from noisy data (D'Adamo *et al.*, 2007; Artana *et al.*, 2012; Cordier *et al.*, 2013; Semaan *et al.*, 2016) and incomplete knowledge of the actual flow dynamics (i.e. unknown initial condition, partially known forcing terms, etc.). Those techniques accurately estimate low-order dynamical systems in the temporal windows on which the data are available. These methods unfortunately experience some limitations for forecasting new states of the system. Furthermore, the physical interpretation of the unresolved velocity component remains difficult since their contribution is distributed in an unknown manner over all the coefficients of the dynamical system and on the error function, when weak dynamical constraint is considered (Artana *et al.*, 2012).

In this work, to take into account the unresolved modes in the surrogate dynamic model, we will rely on a recently proposed stochastic framework (Mémin, 2014; Resseguier *et al.*, 2017*a*). In this context, an advection of the large-scale component due to the action of the unresolved random component emerges naturally, together with an inhomogeneous nonstationary diffusion. This will lead us to consider corrective advection and diffusion terms driven by the turbulence inhomogeneity whose local effects can now be physically interpreted.

After presenting the stochastic model in §2, we describe in §3 the derivation of the associated POD reduced-order model. Furthermore, we propose a method to estimate the additional components of the dimensional reduced system from the residual velocity. Then, the data benchmarks are detailed in §4. From the estimated additional components, we analyse in §5 the influence of the residual velocity on the large-scale flow and reconstruct the temporal modes of the reduced-order models.

2 Dynamics stochastic modelling

The proposed stochastic principle relies on a Lagrangian random description of the flow velocity:

$$\frac{\mathrm{d}\boldsymbol{X}_t}{\mathrm{d}t} = \boldsymbol{w}(\boldsymbol{X}_t, t) + \dot{\boldsymbol{\eta}}(\boldsymbol{X}_t, t). \tag{2.0.1}$$

The first right-hand term, $\boldsymbol{w}$, stands for the large-scale velocity component. It is a smooth component along time. For turbulent flows, it is associated with a much larger time-scale than the unresolved small-scale velocity component. This latter, $\dot{\boldsymbol{\eta}} = \mathrm{d}\boldsymbol{\eta}/\mathrm{d}t$, is associated with fast modes that are rapidly decorrelating at the resolved time scale. Based on this observation, we will assume that such a component can be ideally represented through a spatially smooth incompressible (divergence-free) Gaussian random field uncorrelated in time. This (possibly inhomogeneous) random field is formally built from an infinite-dimensional Brownian motion. It is associated with a covariance tensor denoted:

$$\boldsymbol{Q}_{ij}(\boldsymbol{x}, \boldsymbol{y}, t, t') = \mathbb{E}(\mathrm{d}\eta_i(\boldsymbol{x}, t)\mathrm{d}\eta_j(\boldsymbol{y}, t')) = \boldsymbol{c}_{ij}(\boldsymbol{x}, \boldsymbol{y}, t)\delta(t - t')\mathrm{d}t. \tag{2.0.2}$$

In the following, the diagonal of the covariance tensor, which plays a central role in our setting, will be denoted as: $\boldsymbol{a}(\boldsymbol{x}) \triangleq \boldsymbol{c}(\boldsymbol{x}, \boldsymbol{x}, t)$. This tensor, that may depend on time, will be referred to as the small-scale variance tensor. It is a symmetric positive definite matrix at all spacial points, $\boldsymbol{x}$ (excluding degenerate cases) with dimension in $m^2.s^{-1}$. It corresponds thus to an eddy viscosity term.

This stochastic formulation is related in spirit to the Lagrangian stochastic models based on Langevin equations that have been intensively used for turbulent dispersion (Sawford., 1986) or in probability density function (PDF) modelling of turbulent flows (Haworth & Pope, 1986; Pope, 1994, 2000). However, here our interest focuses more on the associated large-scale Eulerian representations of the flow dynamics. This Eulerian description of the resolved velocity component is obtained through a formulation of the Reynolds transport theorem adapted to such a stochastic flow.

2.1 Stochastic conservation equations

Considering the flow decomposition (2.0.1), the rate of change of a scalar quantity (in the absence of random forcing) within a material volume is given by the following expression (Mémin, 2014; Resseguier *et al.*, 2017*a*):

$$\frac{\mathrm{d}}{\mathrm{d}t}\int_{V(t)} q\ \mathrm{d}\boldsymbol{x} = \int_{V(t)} \left(\frac{\partial q}{\partial t} + \boldsymbol{\nabla}\cdot(q\boldsymbol{w}^*) - \boldsymbol{\nabla}\cdot\left(\frac{1}{2}\boldsymbol{a}\boldsymbol{\nabla}q\right) + \dot{\boldsymbol{\eta}}\cdot\boldsymbol{\nabla}q\right)\mathrm{d}\boldsymbol{x}, \tag{2.1.1}$$

where the effective advection velocity is given as:

$$\boldsymbol{w}^* \triangleq \boldsymbol{w} - \frac{1}{2}\big(\boldsymbol{\nabla}\cdot\boldsymbol{a}\big)^T. \tag{2.1.2}$$

Equation (2.1.1) provides a stochastic representation of the so-called Reynolds transport theorem. It is important to outline that at a given grid point, q is a random value which depends among other things on the Brownian component of the particles flowing through that point. The second term corresponds to the large-scale advection by an effective drift, $\boldsymbol{w}^*$, that includes a contribution related to the divergence of the small-scale velocity variance tensor (2.1.2). The third term is a diffusion expressing the mixing effect exerted by the small-scale velocity component. The final term corresponds to the scalar advection by the small-scale velocity field. From this expression a conservation of an extensive property, $\int_{V(t)} q$, such as mass or internal energy (neglecting diabatic and compressive effects) reads immediately as the following intensive property evolution equation

$$\frac{\partial q}{\partial t} + \boldsymbol{\nabla}\cdot(q\boldsymbol{w}^*) + \dot{\boldsymbol{\eta}}\cdot\boldsymbol{\nabla}q = \boldsymbol{\nabla}\cdot\left(\frac{1}{2}\boldsymbol{a}\boldsymbol{\nabla}q\right). \tag{2.1.3}$$

As the right-hand term is a smooth temporal component, we observe immediately that the Brownian terms associated, on the one hand, to the scalar temporal variation and, on the other hand, to the small-scale advection necessarily compensate each other. A fluid with a constant density ρ, requires naturally a divergence-free constraint on the effective advection:

$$0 = \boldsymbol{\nabla} \cdot \dot{\boldsymbol{\eta}}, \tag{2.1.4}$$

$$0 = \boldsymbol{\nabla} \cdot \boldsymbol{w}^* = \boldsymbol{\nabla} \cdot \left(\boldsymbol{w} - \frac{1}{2} (\boldsymbol{\nabla} \cdot \boldsymbol{a}) \right). \tag{2.1.5}$$

This is the case we are dealing with in this study. The two constraints (2.1.4-2.1.5) correspond to the incompressibility conditions associated with the stochastic representation. For isochoric flows with variable density as in geophysical fluid dynamics, interested readers can refer to Resseguier *et al.* (2017*a*,*b*,*c*).

2.2 Navier-Stokes equations associated with a stochastic representation of the small-scales

Similarly to the Newton second law, a dynamical balance between the temporal differentiation of the stochastic momentum, $\rho \mathrm{d}\boldsymbol{X}_t$, and the action of the forces is assumed. Applying the stochastic representation of the Reynolds transport theorem (2.1.1) leads to the following Navier-Stokes equations (Mémin, 2014):

$$\frac{\partial \boldsymbol{w}}{\partial t} + (\boldsymbol{w}^* \cdot \boldsymbol{\nabla}) \boldsymbol{w} = -\frac{1}{\rho} \boldsymbol{\nabla} p + \sum_{i,j=1}^{d} \frac{\partial}{\partial x_i} \left(\frac{1}{2} \boldsymbol{a}_{ij} \frac{\partial \boldsymbol{w}}{\partial x_j} \right) + \nu \triangle \boldsymbol{w}. \tag{2.2.1}$$

This equation corresponds to the large-scale momentum equation. This expresssion differs from the classical Reynolds decomposition formulation mainly by the introduction of both a large-scale dissipation term and a correction term in the large-scale advection. The dissipative term plays a role that is similar to the eddy viscosity models introduced in classical large scale representations (Bardina *et al.*, 1980; Lilly, 1992; Smagorinsky, 1963) or to the spectral vanishing viscosity (Karamanos & Karniadakis, 2000; Pasquetti, 2006; Tadmor, 1989). It is also akin to numerical regularization models considered in implicit models (Aspden *et al.*, 2008; Boris *et al.*, 1992; Lamballais *et al.*, 2011). The small-scale stochastic representation principle is nevertheless more general as it does not rely on *a priori* fixed shapes of the subgrid tensor (e.g. Boussinesq assumption) nor does it presuppose a given numerical scheme (e.g. implicit models). The subgrid term takes a general diffusion form whose matrix coefficients are given by the small-scale variance tensor. The diffusion principal directions are thus aligned with this tensor principal directions.

The advection correction term is much less intuitive. It is related here to an advection bias due to the inhomogeneity of the small-scale variance tensor. This corresponds to the eddy-induced velocity introduced for tracer mean transport in oceanic or atmospheric circulation models (Andrews & McIntyre, 1976; Gent *et al.*, 1995) and more generally to the *turbophoresis* phenomenon associated with small-scale inhomogeneity, which drives inertial particles toward the regions of lower diffusivity (Brooke *et al.*, 1992; Caporaloni *et al.*, 1975; Reeks, 1983; Sehmel, 1970). Qualitatively, this drift correction can be understood as follow. Fluid parcels with higher turbulent kinetic energy (TKE) move faster. It ensues that at large scales, areas associated with maximum of TKE spread whereas areas associated with minimum of TKE shrink. Hence, a large-scale drift oriented toward these maxima/minimum emerges. This orientation suggests an anticorrelation with the TKE gradient. Since the turbulent velocity variations are multidimensional, they are better described by the variance tensor. The drift correction is consequently proportional to the opposite of the variance tensor divergence. For homogeneous turbulence, the small-scale variance tensor is constant and this corrective advection does not come into play. It can be noted that this advection correction is of the same form as the one proposed in Caporaloni *et al.* (1975); Macinnes & Bracco (1992); Reeks (1983).

The small-scale random field can be freely defined and be in a shape that goes from isotropic stationary models up to inhomogeneous non-stationary random fields. However, in the inhomogeneous case (such

as the Smagorinsky model) the advection correction term comes into play. A stochastic representation of the unresolved scales differ thus significantly from classical large-scale modelling. It relies on less strict assumptions, which enable to cope naturally with inhomogeneous anisotropic turbulence.

This stochastic representation relies on a scale gap assumption, which is coherent with deterministic justifications of the eddy viscosity (Kraichnan, 1987). The stochastic transport expression (2.1.1) and the momentum equation (2.2.1) provide the foundations of a physically relevant large-scale fluid dynamics formulation. It opens a new paradigm for large-scale modelling adapted to turbulence inhomogeneity in involving a general subgrid diffusion together with a small-scale drift correction. In the next section, we will rely on this model for the construction of reduced-order dynamical systems.

3 Reduced-order models

Dimensional reduction techniques enable the constitution of simplified lower dimensional representations of partial differential equations (PDE). They are usually specified from a Galerkin projection onto data-based dedicated basis. The proper orthogonal decomposition, also called Empirical Orthogonal Functions (EOF) in geophysics, is one of those methods for turbulent flows. In §3.1 the POD model reduction is briefly presented. Then, in §3.2 we introduce the derivation of the reduced-order model from the stochastic representation principle described in §2. In §3.3, different characteristic time scales are introduced for the different modes, leading to the concept of modal characteristic time steps. Finally, in §3.4 a precise specification of the small-scale variance tensor is proposed with two different estimation methods.

3.1 POD model reduction

POD reduced-order models rely on the linear decomposition of the velocity $\boldsymbol{w}$ on a reduced number of orthogonal spatial modes (Holmes *et al.* (1996)):

$$\boldsymbol{w}(\boldsymbol{x},t) \approx \sum_{i=0}^{n} b_i(t)\boldsymbol{\phi}_i(\boldsymbol{x}). \tag{3.1.1}$$

The number of modes, n, is assumed to be much lower than the state space dimension. The functions $(\boldsymbol{\phi}_i(\boldsymbol{x}))_{1\leqslant i\leqslant N}$ encoding the spatial flow variations are referred to as *topos* and are computed from a Karunen-Loeve decomposition on a series of $N+1$ available velocity snapshots. The *topos* are sorted by decreasing order of the snapshots empirical covariance eigenvalues: $\lambda_1 > ... > \lambda_N$. The $(b_i(t))_{1\leqslant i\leqslant N}$ denote the temporal modes; they are called *chronos*. The *chronos* are the eigenvectors of the spatially averaged temporal correlation matrix, whereas the *topos* constitute the eigenvectors of the temporally averaged spatial correlation matrix. They are both computed from the snapshots covariance. Function ϕ_0 corresponds to the time average velocity and $b_0 \triangleq \lambda_0 \triangleq 1$. We also denote by T the time between the first and the last snapshot. The Navier-Stokes equations can be written in the general following form:

$$\frac{\partial \boldsymbol{w}}{\partial t} = \boldsymbol{I} + \boldsymbol{L}(\boldsymbol{w}) + \boldsymbol{C}(\boldsymbol{w},\boldsymbol{w}), \tag{3.1.2}$$

where $\boldsymbol{L}$ and $\boldsymbol{C}$ stand respectively for linear and bilinear differential operators. The first term, $\boldsymbol{I}$, gathers the pressure and the external forces such as gravity. The second one, $\boldsymbol{L}$, includes the molecular friction term and possibly the Coriolis force. The last one, $\boldsymbol{C}$, encodes the nonlinear advection term. Projecting this PDE on each *topos* leads to:

$$\frac{\mathrm{d}b_i}{\mathrm{d}t} = \underbrace{\left(\int_\Omega \boldsymbol{\phi}_i \cdot \boldsymbol{I}\right)}_{\triangleq i_i} + \sum_{p=0}^{n} \underbrace{\left(\int_\Omega \boldsymbol{\phi}_i \cdot \boldsymbol{L}(\boldsymbol{\phi}_p)\right)}_{\triangleq l_{p,i}} b_p + \sum_{p,q=0}^{n} \underbrace{\left(\int_\Omega \boldsymbol{\phi}_i \cdot \boldsymbol{C}(\boldsymbol{\phi}_p,\boldsymbol{\phi}_q)\right)}_{\triangleq c_{p,q,i}} b_p b_q. \tag{3.1.3}$$

Due to nonlinearity, the temporal modes strongly interact with one another. In particular, even though the original model (with $n = N$) is computationally stable for moderate Reynolds number, a strongly reduced model ($n \ll N$) appears unstable in general. A frequency shift is also often observed. Those artefacts are extensively documented in the literature (Artana *et al.*, 2012; Aubry *et al.*, 1988; Rempfer & Fasel, 1994; Östh *et al.*, 2014; Protas *et al.*, 2015). The introduction of a damping eddy viscosity term to mimic the truncated modes' dissipation leads to a modified linear term in (3.1.3). Unfortunately, as this term is built on empirical grounds its precise form is difficult to justify. Furthermore, its parametrization has to be tuned for each simulation to achieve good results. When large wake domains are considered the influence of the pressure term (and of the boundaries) is in general negligible (Deane *et al.*, 1991; Ma *et al.*, 2002; Noack *et al.*, 2005). We will also rely on this assumption, although several authors have shown that neglecting the pressure term was a source of uncertainty regarding an accurate representation of the flow dynamics (Kalb & Deane, 2007; Noack *et al.*, 2005). To take into account the effect of the outflow boundary, corrective terms are introduced by some authors through modifications of the linear (Galetti *et al.*, 2007) or quadratic terms (Noack *et al.*, 2005).

3.2 Reduced-order modelling associated with the stochastic representation

To overcome the difficulties evoked previously, we propose to derive the reduced-order model from the stochastic representation principle described previously. To account for the effect due to the modal truncation, we will assume that the whole field $\boldsymbol{u} = \boldsymbol{w} + \dot{\boldsymbol{\eta}}$ can be decomposed in such a way that the large-scale component lives on the subspace endowed with the reduced POD basis $\boldsymbol{w} = \sum_{i=0}^{n} b_i \boldsymbol{\phi}_i$ while realisations of the small-scale component belong to the orthogonal complement subspace $\dot{\boldsymbol{\eta}} = \sum_{i=n+1}^{N} b_i \boldsymbol{\phi}_i$. Since $\boldsymbol{\nabla \cdot u} = 0$, for all i, $\boldsymbol{\nabla} \cdot \phi_i = 0$ and, then, $\boldsymbol{\nabla \cdot w} = 0$. The dynamics of the large-scale component, $\boldsymbol{w}$, is given by the incompressible Navier-Stokes equations (2.2.1). Projecting this equation onto the *topos* $\boldsymbol{\phi}_i$ leads to:

$$\frac{\mathrm{d}b_i}{\mathrm{d}t} = i_i + \left(\boldsymbol{l}_{\bullet i} + \breve{\boldsymbol{f}}(\boldsymbol{a})_{\bullet i}\right)^T b + b^t \boldsymbol{c}_{\bullet\bullet i} b \ , \tag{3.2.1}$$

$$\text{where } \breve{\boldsymbol{f}}(\boldsymbol{a})_{j,i} \triangleq \int_\Omega \sum_{k=1}^{d} \boldsymbol{\phi}_i^{(k)} \cdot \left(\underbrace{-\frac{1}{2}(\boldsymbol{\nabla \cdot a})\boldsymbol{\nabla}\phi_j^{(k)}}_{\text{Advection}} + \underbrace{\boldsymbol{\nabla} \cdot \left(\frac{1}{2}\boldsymbol{a}\boldsymbol{\nabla}\phi_j^{(k)}\right)}_{\text{Diffusion}} \right). \tag{3.2.2}$$

Let us note that $\breve{\boldsymbol{f}}(\boldsymbol{a})$ is linear and is the only function that depends on the variance tensor $\boldsymbol{a}$. This system includes now a natural small-scales dissipation mechanism, through the diffusion term. But it also corrects the frequency shift through the additional advective term brought by the variance tensor inhomogeneity. To fully define this system, we need to specify the small-scale variance tensor $\boldsymbol{a}$. This issue is developed in subsection 3.4. But before that, we will elaborate further on the choice of the characteristic times related to the modal truncation.

3.3 Time scale characterisation

Very efficient flow simulations are obtained by reducing as much as possible the number of modes of the associated surrogate model. An even higher efficiency can be obtained by increasing the evolution time step. This time step can be naturally chosen as a single constant for the whole system. However, as we shall see, different characteristic time scales can be fixed for the different modes, leading to the concept of modal characteristic time steps.

3.3.1 Single time step

As long as the resolved modes, representing $\boldsymbol{w}$, are smooth w.r.t. time, the assumption pertaining to our reduced model construction is valid. The time-step must thus be fixed as the largest value that guarantees

that all the *chronos* remain smooth. The characteristic time scale associated with the fastest resolved mode (which is often the least energetic mode) is a good target for that purpose. This time scale is associated with the highest frequency of the *chronos* Fourier modes. Quantitatively, the Shannon-Nyquist theorem provides us with a natural upper bound to fix its value. This theorem states that a function can be sampled, without loss of information, if the sampling frequency is two times bigger than the largest frequency of the original function. Otherwise, the sampled function undergoes an aliasing artifact characterized by a folding of the Fourier spectrum and a loss of regularity. We will thus assume that the required regularity condition is fulfilled if the modes are not affected by aliasing phenomena. Since the evolution equations are quadratic, a sufficient condition thus reads:

$$\frac{1}{\Delta t} \geqslant 4 \max_{i \leqslant n} \left(f_{max} \left(b_i \right) \right). \tag{3.3.1}$$

where $f_{max}\left(b_i\right)$ is the maximum frequency of the i-th mode. Aliasing takes place in the unresolved temporal modes, which are associated with smaller time scales. However, the stochastic representation is precisely built from a decorrelation assumption of the small-scale unresolved part of the velocity. A strong subsampling of those components strengthens further the decorrelation property of the unresolved modes.

3.3.2 Modal characteristic times

The resolved *chronos* are associated with different time scales. Hence, the previous criterion can be immediately extended to get a characteristic time scale attached to each *chronos*, b_i:

$$\frac{1}{\Delta t_i} \geqslant 4 f_{max} \left(b_i \right). \tag{3.3.2}$$

A modal variance tensor field for each *chronos* can now be defined as

$$\boldsymbol{a}^{(i)}(\boldsymbol{x}) \stackrel{\triangle}{=} \Delta t_i \mathbb{E}\left\{ \dot{\boldsymbol{\eta}} \dot{\boldsymbol{\eta}}^T \right\}(\boldsymbol{x}) = \frac{\Delta t_i}{\Delta t} \tilde{\boldsymbol{a}}(\boldsymbol{x}) \text{ with } \tilde{\boldsymbol{a}}(\boldsymbol{x}) = \Delta t \ \mathbb{E}\left\{ \dot{\boldsymbol{\eta}} \dot{\boldsymbol{\eta}}^T \right\}(\boldsymbol{x}). \tag{3.3.3}$$

The modal variance tensor $\boldsymbol{a}_i$ corresponds to the small-scale velocity variance during a given time step at the time-scale of the *Chronos* b_i (i.e. it corresponds to an eddy viscosity associated with the neglected modes expressed with respect to the characteristic time associated with b_i). The *chronos* evolution equation (3.2.1) thus becomes:

$$\frac{\mathrm{d}b_i}{\mathrm{d}t} = i_i + \left(\boldsymbol{l}_{\bullet i} + \frac{\Delta t_i}{\Delta t} \breve{\boldsymbol{f}}(\tilde{\boldsymbol{a}})_{\bullet i} \right)^T b + b^t \boldsymbol{c}_{\bullet\bullet i} b. \tag{3.3.4}$$

The time step Δt corresponds in practice to the simulation time step.

3.4 Estimation of the small-scale variance tensor

The full definition of the reduced-order model requires a precise specification of the small-scale variance tensor. We compare here two different estimation methods for this tensor. A first method will rely on a stationarity assumption while a second technique will allow us to define a time-varying tensor.

3.4.1 Stationary small-scale variance tensor

This case corresponds to the model developed in Mémin (2014). The small-scale velocity variance, $\boldsymbol{a}/\Delta t$ can be computed through a temporal averaging of the residual velocity second moment $(\boldsymbol{u}-\boldsymbol{w})(\boldsymbol{u}-\boldsymbol{w})^T(t_i)$ at all spatial locations. This simple scheme thus provides a representation of a spatially varying stationary variance tensor.

3.4.2 Small-scale variance tensor in the chronos subspace

A stationary model has obvious limitations in terms of turbulence intermittency modelling. A time dependent variance tensor is nevertheless more involved to estimate as in this case only a single realization of the small-scale velocity trajectory, $(\boldsymbol{u}(\boldsymbol{x},t)-\boldsymbol{w}(\boldsymbol{x},t))$, is available. However considering a temporal basis it is possible to estimate, at a fixed point, the matrix coefficients, $\boldsymbol{z}_i(\boldsymbol{x})$, of the tensor, $\boldsymbol{a}(\boldsymbol{x},t)$ (Genon-Catalot *et al.*, 1992). We term those coefficients the *diffusion modes*, as they correspond to a modal decomposition of the principal diffusion directions. With the *chronos* reduced basis we get:

$$\tilde{\boldsymbol{a}}(\boldsymbol{x},t)=\sum_{j=0}^{n} b_j(t)\boldsymbol{z}_j(\boldsymbol{x}). \tag{3.4.1}$$

Using the orthogonality of the *Chronos*, $\int_0^T b_k b_l \mathrm{d}t=\delta_{kl}\lambda_k T$, leads to:

$$\boldsymbol{z}_j(\boldsymbol{x}) \quad = \quad \int_0^T \frac{b_j(t)}{T\lambda_j}\tilde{\boldsymbol{a}}(\boldsymbol{x},t)\mathrm{d}t \quad \approx \quad \frac{\Delta t}{N+1}\sum_{k=0}^{N}\frac{b_j(t_k)}{\lambda_j}(\boldsymbol{u}-\boldsymbol{w})(\boldsymbol{x},t_k)((\boldsymbol{u}-\boldsymbol{w})(\boldsymbol{x},t_k))^T, \tag{3.4.2}$$

where $N=\frac{T}{\Delta t}$. It can be noticed that keeping only the zero-diffusion mode and canceling the others: $z_i=0,\ \forall i\geqslant 1$, brings us back to the stationary variance tensor model. The non-zero modes introduce a time varying variance. Yet, it is important to outline that the reduced-order model (3.2.1) remains a quadratic autonomous system. As a matter of fact from (3.4.1), we get the following system:

$$\frac{\mathrm{d}b_i}{\mathrm{d}t}=i_i+\boldsymbol{l}_{\bullet i}^T b+b^T\left(\boldsymbol{c}_{\bullet\bullet i}+\boldsymbol{f}_{\bullet\bullet i}\right)b, \text{ where } f_{pqi}\triangleq\frac{\Delta t_i}{\Delta t}\breve{f}_{qi}\left(\boldsymbol{z}_p\right). \tag{3.4.3}$$

4 Flow configuration and numerical simulations

To evaluate the pertinence of the modelling developed in the previous section for the specification of a low order dynamical system and to analyse the contribution of the small-scale component, we consider three-dimensional incompressible flows past a circular cylinder at Reynolds number $Re=300$ and $Re=3900$. We performed direct numerical simulations (DNS) using Incompact3d, a high-order flow solver, based on the discretization of the incompressible Navier–Stokes equations with finite-difference sixth-order schemes on a cartesian mesh (Laizet & Lamballais, 2009). A second-order Adams-Bashforth scheme was used for the time advancement. The incompressibility condition is treated with a fractional step method based on the resolution of a Poisson equation in spectral space, allowing here for the velocity field the use of periodic boundary conditions in the two lateral directions y and z. A constant flow is imposed at the inlet of the computational domain and a simple convection equation is solved at the exit. Using the concept of the modified wavenumber, the divergence free condition is ensured up to machine accuracy. The pressure field is staggered from the velocity field by half a mesh to avoid spurious oscillations. The modelling of circular cylinder of diameter D inside the computational domain was performed here with a simple Immersed Boundary Method (IBM). It is based on a direct forcing to ensure zero velocities boundary condition at the wall and inside the solid body. We also used data extracted from a large-eddy numerical simulation (LES) performed by Parnaudeau *et al.* (2008) using a former version of Incompact3d. This code solved incompressible Navier–Stokes equations on a regular cartesian grid in nonstaggered configuration and using the customized IBM technique of Parnaudeau *et al.* (2004) to avoid discontinuities on the velocity field, leading to the creation of spurious oscillations when high-order centered schemes are used. This LES was carried out with a high spatial resolution, close to the one expected for a DNS, and with the subgrid-scale model proposed by Métais & Lesieur (1992) combined with a fixed filter length estimated as the cubic root of the mesh volume.

Three different cases were considered: a DNS at Reynolds number $Re=300$, a high resolution LES (HR LES) at Reynolds number $Re=3900$ (Parnaudeau *et al.*, 2008) and a low resolution DNS (LR DNS)

Case	Re	$(L_x \times L_y \times L_z)/D$	$n_x \times n_y \times n_z$	Snapshots	Shedding cycles
DNS	300	$20 \times 20 \times 0.5$	$512 \times 321 \times 8$	3999	80
HR LES	3900	$20 \times 20 \times \pi$	$961 \times 960 \times 48$	219	5
LR DNS	3900	$20 \times 20 \times \pi$	$961 \times 960 \times 48$	2499	80

Table 1: Summary of simulations and of extracted data.

at Reynolds number $Re = 3900$. We performed the DNS at Reynolds number $Re = 300$ on a domain extending over $20D \times 20D \times 0.5D$ with $512 \times 321 \times 8$ points in the streamwise, perpendicular and spanwise directions, respectively. This reduced spanwise length corresponds to the minimum domain size usable with Incompact3d and led to a three dimensional wake flow simulation with a very short periodicity in the spanwise direction. This choice was done to reduce the computational cost and to simulate a longer time series, necessary for the POD analysis. The simulation was run on $N = 3999$ time steps to observe 80 vortex shedding cycles. The high resolution LES of Parnaudeau *et al.* (2008) we used was computed on a domain size of $20D \times 20D \times \pi D$ with $960 \times 960 \times 48$ points in the streamwise, perpendicular and spanwise directions, respectively. We extracted from this simulation 219 equidistant snapshots over 5 vortex shedding cycles. In order to have longer time series we performed a low resolution DNS for the same Reynolds number $Re = 3900$ and with the same domain size and mesh grid. This DNS was run on 2499 time steps to observe 80 vortex shedding, with the last parallel version of Incompact3d (Laizet & Li, 2011). Since the new version of Incompact3d did not implement the subgrid-scale model used in the study of Parnaudeau *et al.* (2008), we performed a low-resolution DNS for the same Reynolds number. The main difference in the results between HR LES and LR DNS are discussed below.

In the following (with the exception of §5.1), non-dimensional quantities are considered, and calculated using the cylinder diameter D and the inflow velocity U_0. Dimensionless quantities will be identified by lower-case symbols, e.g. (x, y, z) for the coordinate system and t for the time. In this frame reference, the inflow velocity vector at $x = 0$ is $(u, v, w) = (1, 0, 0)$ and the cylinder is located at $(x, y, z) = (5, 0, z)$. Details of the three cases are provided in table 1. Figure 1 shows the spanwise vorticity component in the plane $z = 0$ for the DNS at Reynolds number $Re = 300$, the high resolution LES at Reynolds number $Re = 3900$ and the low resolution DNS at Reynolds number $Re = 3900$, respectively. At Reynolds number $Re = 300$ and due to the quasi two-dimensional configuration of the simulation, there are only few small-scale features. Most of the energy is gathered in the large-scale vortical structures. In this regime two topos modes are sufficient to describe faithfully the flow. At Reynolds number $Re = 3900$, a sustained turbulence can be observed in the far wake of the cylinder and in the recirculation zone just behind the cylinder. The boundary layer on the body is laminar and transition to turbulence takes place in the shear layers. The near wake flow is mostly driven by those two shear layers (Ma *et al.*, 2000). Their oscillations trigger the Von Karman vortex shedding and determine the size of the recirculation area. For this wake flow regime a higher number of modes must be kept. From figure 1 we can compare the predictions of both simulations at Reynolds number $Re = 3900$. It is worth noting that HR LES exhibits a statistical behaviour consistent with experimental measurements (Parnaudeau *et al.*, 2008), especially in the very near wake for the prediction of the length of recirculation zone. On the contrary, LR DNS yields shorter formation length close to the one obtained at higher Reynolds number, i.e. for $Re \sim 10000$. This behaviour of low resolution wake flow simulations is classical and associated with the so called V-shape of the mean streamwise velocity profiles for $x \leq 8$ (Ma *et al.*, 2000). Hence, both simulations provide distinct vorticity distributions in the very near wake. Farther downstream, i.e. for $x \geq 8$, such pronounced differences are less noticeable. LR DNS exhibits some wiggles, which seem to increase sligthly the vorticity spreading along the wake.

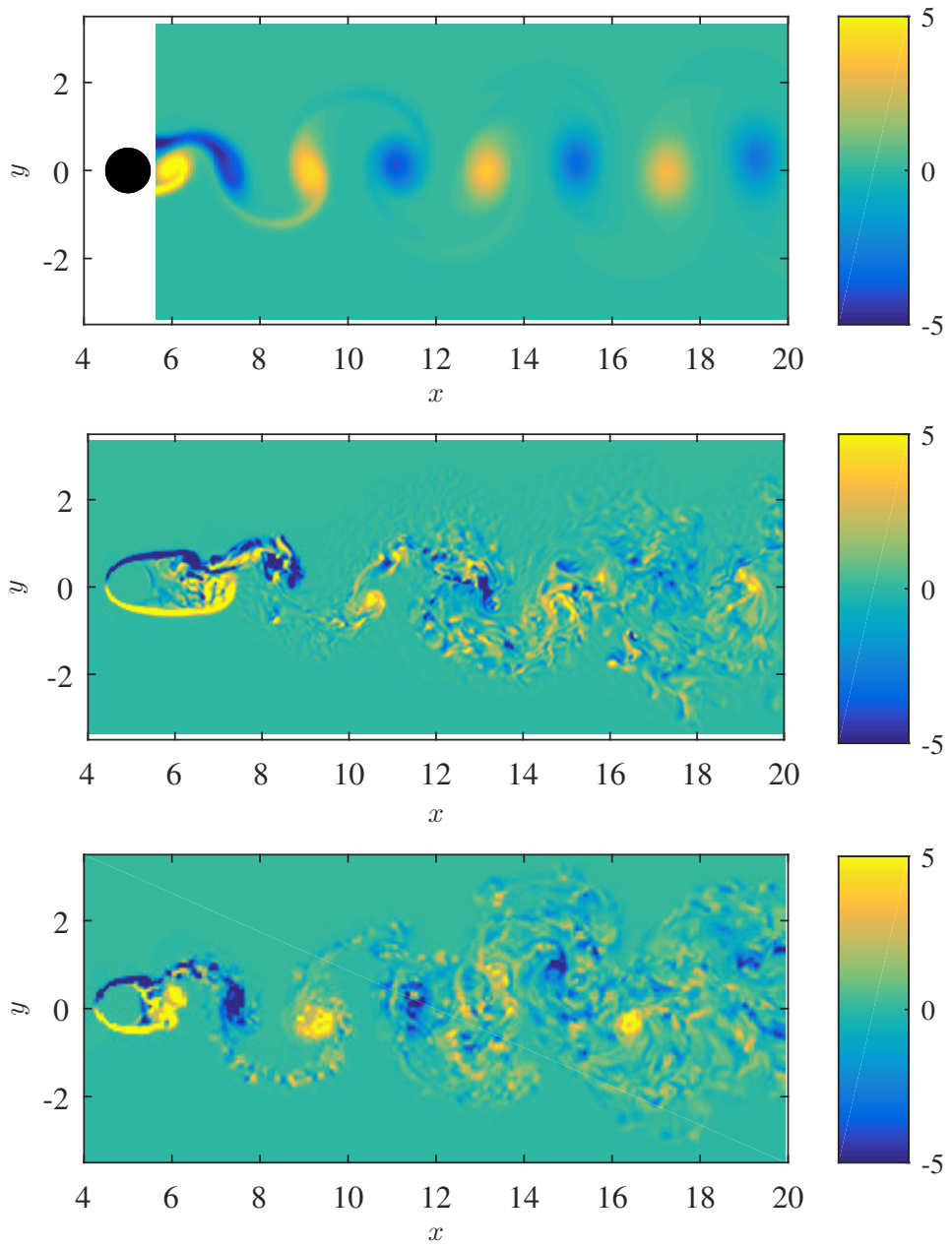

Figure 1: Spanwise vorticity componant in a circular cylinder wake flow at Reynolds number, from top to bottom, $Re = 300$ (DNS), $Re = 3900$ (high resolution LES, Parnaudeau *et al.* (2008)) and $Re = 3900$ (low resolution DNS), respectively.

5 Diffusion modes results

We now apply the novel POD modelling based on a stochastic small-scale representation presented in §3 to the cylinder flow configuration described in §4. The reduced-order dynamics of the cylinder wake flow is known to be sensitive to the unresolved small-scale velocity component. In §5.1, the small-scale energy and anisotropy is linked to small-scale diffusion modes. Assessment of the stochastic modelling is then performed in the following at the Reynolds number $Re = 300$ and $Re = 3900$, respectively. In §5.2, contributions of small-scale diffusion modes to large-scale flow are described and interpreted to determine which physical mechanisms of the wake flow are concerned. In §5.3, we assess the performance of the subgrid term that was introduced by the stochastic representation of the small-scales by comparing the *chronos* trajectories to the reference.

5.1 Estimation and decomposition of the turbulent velocity components

It can be noticed in the decomposition (3.4.1), that the diffusion modes $\boldsymbol{z}_i(x)$ are $d \times d$ symmetric matrices (with $\boldsymbol{z}_i = 0$ for $i > 0$ in the stationary case) at all spatial points. They can be diagonalized in a local orthonormal basis. Let us note however this decomposition does not ensure that $\boldsymbol{a}(x,t) = \sum_{k=0}^{n} b_k(t)\boldsymbol{z}_k(x)$ is positive definite since $b_i(t)$ takes positive and negative values. In practice though the stationary coefficient dominates largely the others (which gives a positive definite estimation), it would be necessary to project the variance tensor on the manifold of positive definite matrices. In the following section, to analyse the small-scale energy and anisotropy we visualize the absolute values of the eigenvalues associated with the matrix modes, $\boldsymbol{z}_i$. Due to *chronos* normalization, the variance tensor diffusion modes must be also normalized by the *chronos*' square root eigenvalues $\sqrt{\lambda_i}$, as:

$$\tilde{\boldsymbol{a}}(x,t) = \sum_{k=0}^{n} \frac{b_k(t)}{\sqrt{\lambda_k}} \left(\sqrt{\lambda_k} z_k(x)\right) \text{ and } \frac{1}{T}\int_0^T \left(\frac{b_k}{\sqrt{\lambda_k}}\right)^2 = 1. \tag{5.1.1}$$

We note this normalization put an even stronger emphasis on the stationary dissipation zero-mode. Then, by (2.1.2) the corrective drift reads

$$\boldsymbol{w}^\star - \boldsymbol{w} = \sum_{k=0}^{n} \frac{b_k(t)}{\sqrt{\lambda_k}}\, \boldsymbol{v}_c^{(k)}(\boldsymbol{x}) \text{ with } \boldsymbol{v}_c^{(k)} = -\frac{1}{2}\boldsymbol{\nabla}\cdot\left(\sqrt{\lambda_k}\boldsymbol{z}_k\right)^T. \tag{5.1.2}$$

Before dealing with *chronos* reconstruction, we propose in §5.1 and 5.2 a new type of POD data analysis involving the information contained in the residual velocity. Algorithm 1 summarizes the steps of our data analysis, including the POD and the diffusion modes computation.

5.2 Small-scale energy density, stationarity and anisotropy

The turbulent kinetic energy density (TKE) was computed by the sum of the diffusion modes eigenvalues, since small-scale TKE is represented (up to a time scale) by the norm of that tensor. The bigger the TKE, the more important the diffusion is. The diffusion zero-mode energy is plotted in figure 2 *(a)* for the circular cylinder wake flow at $Re = 300$, with two POD modes and in the plane $z = 0$. The other diffusion modes are much weaker (not shown) and the small-scale velocities component is thus almost stationary. The colormap yields regions of high TKE in the recirculation zone and in an arrow shape just downstream in the transitional region, i.e. for $7 \leq x \leq 10$.

To measure small-scale anisotropy, we computed the ratio between largest and smallest eigenvalues, corresponding to the condition number of the local small-scale velocity variances. The bigger this quantity the more aligned toward the first local proper direction the small-scale velocity is, i.e. the more anisotropic the small-scale velocity and the diffusion are. Figure 2 *(b)* shows the colormap of this quantity for the circular cylinder wake flow at $Re = 300$. In regions where the unresolved velocity component is largely

Algorithm 1 POD and diffusion modes data analysis

function STOCHASTIC_POD_ANALYSIS$(n, \boldsymbol{v}(\boldsymbol{x}, t_0), ..., \boldsymbol{v}(\boldsymbol{x}, t_N)))$

1. Usual POD
   Resolved velocity component
   $$\boldsymbol{w}(\boldsymbol{x}, t) = \sum_{i=0}^{n} b_i(t)\boldsymbol{\phi}_i(\boldsymbol{x}). \tag{5.1.3}$$
2. Optimal time step
   $$\frac{1}{\Delta t} = 4 \max_{i \leqslant n} \left(f_{max}\left(b_i\right)\right). \tag{5.1.4}$$
3. Diffusion modes analysis: study of the residual velocity component influence
   - Residual velocity component
     $$\boldsymbol{v} - \boldsymbol{w}. \tag{5.1.5}$$
     Decomposition of the residual velocity influence
   - **for** $j = 0$ to n **do**
     Component of the residual velocity influence associated with the time variability of the *chronos* b_j (note that $b_0 = \lambda_0 = 1$)
     - Diffusion mode computation
       Projection of the squared residues on the resolved *chronos* b_j
       $$\boldsymbol{z}_j(\boldsymbol{x}) = \frac{\Delta t}{N+1} \sum_{k=0}^{N} \frac{b_j(t_k)}{\lambda_j} (\boldsymbol{u} - \boldsymbol{w})(\boldsymbol{x}, t_k)((\boldsymbol{u} - \boldsymbol{w})(\boldsymbol{x}, t_k))^T. \tag{5.1.6}$$
     - Analysis of the diffusion of the resolved velocity $\boldsymbol{w}$ by the residual velocity
       * Local diagonalization of the symmetric matrix $\boldsymbol{z}_i(\boldsymbol{x})$
         $$\sqrt{\lambda_j}\boldsymbol{z}_j(\boldsymbol{x}) = \boldsymbol{P}_j(\boldsymbol{x})\boldsymbol{\Lambda}^{(j)}(\boldsymbol{x})\boldsymbol{P}_j^T(\boldsymbol{x}), \tag{5.1.7}$$
         with
         $$\boldsymbol{P}_j(\boldsymbol{x})\boldsymbol{P}_j(\boldsymbol{x})^T = \boldsymbol{P}_j(\boldsymbol{x})^T\boldsymbol{P}_j(\boldsymbol{x}) = \mathbb{I}_d \text{ and } \boldsymbol{\Lambda}_{pq}^{(j)}(\boldsymbol{x}) = \delta_{pq}\boldsymbol{\Lambda}_{pp}^{(j)}(\boldsymbol{x}). \tag{5.1.8}$$
       * Inhomogeneity of the turbulent diffusion of the resolved velocity (proportional to the small-scale kinetic energy)
         $$\sum_{p=1}^{d} \left| \boldsymbol{\Lambda}_{pp}^{(j)}(\boldsymbol{x}) \right|. \tag{5.1.9}$$
       * Anisotropy of the turbulent diffusion of the resolved velocity (equal to the anisotropy of the small-scale kinetic energy)
         $$\frac{\max_p \left| \boldsymbol{\Lambda}_{pp}^{(j)}(\boldsymbol{x}) \right|}{\min_p \left| \boldsymbol{\Lambda}_{pp}^{(j)}(\boldsymbol{x}) \right|}. \tag{5.1.10}$$
     - Corrective drift
       $$\boldsymbol{v}_c^{(j)}(\boldsymbol{x}) = -\frac{1}{2}\boldsymbol{\nabla} \cdot \left(\sqrt{\lambda_j}\boldsymbol{z}_j\right)^T (\boldsymbol{x}). \tag{5.1.11}$$
       * Vorticity of the corrective drift
         $$\boldsymbol{\nabla} \times \boldsymbol{v}_c^{(j)}. \tag{5.1.12}$$
       * Divergence of the corrective drift
         $$\boldsymbol{\nabla} \cdot \boldsymbol{v}_c^{(j)}. \tag{5.1.13}$$
   - **end for**

end function

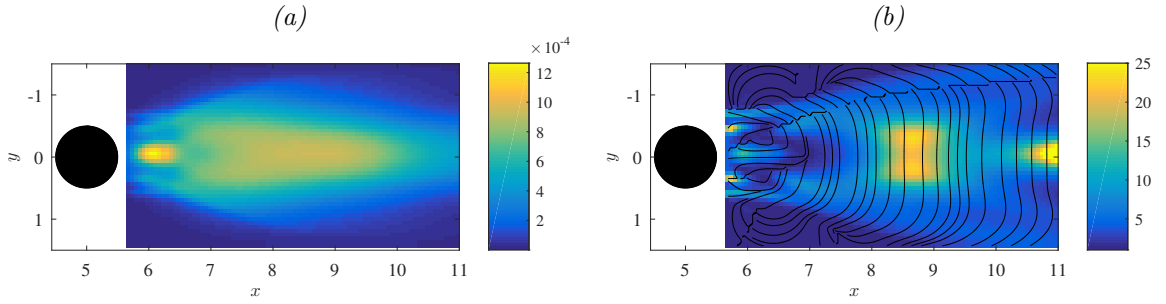

Figure 2: Local spectral representations of the matrix $\boldsymbol{a}$ in a cylinder wake flow at $Re = 300$, for $n = 2$ POD modes and in the plane $z = 0$: *(a)*, Turbulent kinetic energy of the diffusion modes $\boldsymbol{z}_0$ (square root of the sum of the squared eigenvalues); *(b)*, Small-scale anisotropy of the diffusion modes $\boldsymbol{z}_0$ (ratio of the absolute value of the largest eigenvalue to the absolute value of the smallest eigenvalue). The streamlines represent the first proper diffusion direction (i.e. the eigenvectors corresponding to the largest eigenvalues of the small-scale variance tensor).

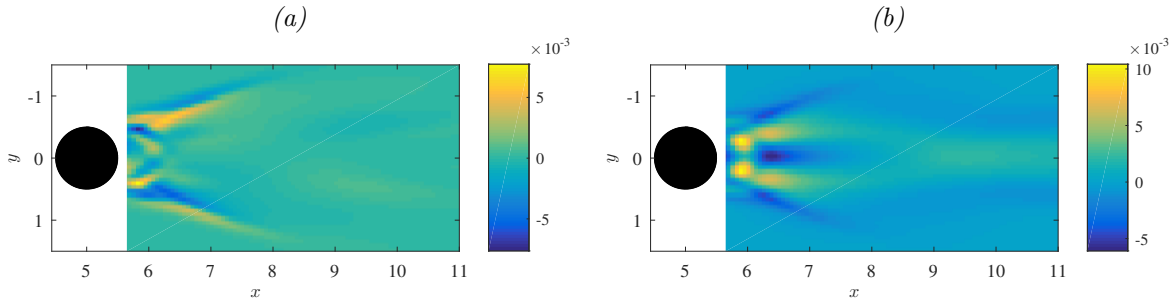

Figure 3: Spanwise vorticity *(a)* and divergence *(b)* of the drift correction $-\frac{1}{2}\left(\boldsymbol{\nabla}\cdot\boldsymbol{a}\right)^T$, for the diffusion zero-mode $\boldsymbol{z}_0$ and $n = 2$ POD modes, in a cylinder wake flow at $Re = 300$.

anisotropic, the small-scale velocity is mainly directed in the direction of the eigenvector associated with the largest eigenvalue of the small-scale variance tensor. The small-scale component imposes a diffusion of the resolved velocity in the same direction. The streamlines in figure 2 *(b)* shows the principal local diffusion directions defined by the largest eigenvectors. The orthogonal to the streamlines would depict the directions of least diffusion of the large-scale velocity by the small-scale component. These directions can be interpreted as the ones of least small-scale uncertainty. The streamlines clearly show the vortex formation region with the symmetric vortex rolling zone. The two pivotal locations at $y = \pm 0.5$ just before station $x = 6$ where both shear layers start to roll into vortices are precisely indicated by high values of the small-scale anisotropy. Downstream, just before station $x = 9$ in the middle of the transitional region, the anisotropy reaches high values in an approximately square area of length D. To this maximum corresponds the zone where vortices detach from the cylinder and reorganise into the Karman vortex street further downstream. Near station $x \approx 11$ at the beginning of this pattern of regular and aligned vortices, small-scale velocity anisotropy is maximum on the centreline.

Another interesting feature of the small-scales stochastic representation principle concerns the emergence of the small-scale effective velocity (2.1.2), also called drift correction, related to the variance tensor inhomogeneity. Though at $Re = 300$, this contribution is weak as the flow is well captured with only

two POD modes, it is nevertheless interesting to observed the velocity component that is induced by the neglected POD modes. In figure 8 we plot the vorticity and divergence of this advection correction term (2.1.2) for the diffusion zero-mode $\boldsymbol{z}_0$. The small-scale vorticity induced by the neglected modes is 3 order of magnitude weaker than the whole flow vorticity (figure 1), which confirms its minor effect on the large-scale flow. However some interesting patterns emerge from those figures. In the divergence map (figure 3 *b*) we observe high divergence zones at station $x = 6$ corresponding to the vortex formation and just downstream at station $x = 6.5$ where the vortices are shed. Convergence zones are also shown at the same station but on the centreline and on both sides just outside of the recirculation region. In the vorticity map (figure 3 *a*) several small-scale vorticity spots take place within the recirculation area, whereas elongated vorticity patterns can be observed, like for the convergence, just outside of the recirculation region. Such flow corrections, though being weak, take place in the region of the flow where physical mechanisms that give rise to vortex shedding are active and may have significant contributions if the flow is sensitive in these regions. One interesting feature, here, is the presence of high values of vorticity, corresponding to the maximum of anisotropy, at the two pivotal locations of the shear layers rolling into vortices.

Then it is of particular interest to analyse how the proposed small-scale stochastic modelling behaves with a higher turbulent wake flow. We then consider the cylinder wake flow at Reynolds number $Re = 3900$ (HR LES). It should be noted that the low number of velocity snapshots available for that case (see table 1) leads to insufficient convergence of the POD modes. To avoid to much wiggles on the diffusion modes results the matrix $\boldsymbol{a}$ was computed only in two-dimensions in fixed z-planes and then averaged along the z-axis. Hence the contribution of the small-scale spanwise velocity component was neglected and the analysis was based on an averaged view of $\boldsymbol{a}$ along the z-axis. Colormaps of the energy density for the diffusion modes $\boldsymbol{z}_0$, $\boldsymbol{z}_1$ and $\boldsymbol{z}_2$ are plotted in figure 4 *(a)*, for 4 POD modes. We observe that the turbulent energy of the diffusion zero-mode is three times larger than for the nonstationary modes. These spatial small-scale energy distributions show that the largest magnitudes are reached at the end of the recirculation region and further downstream in the transitional region. Examination of the small-scale anisotropy spatial distribution together with the streamlines of the principal local diffusion directions plotted in figure 4 *(b)*, indicates for $\boldsymbol{z}_0$ diffusion mode the two pivotal regions where the shear layers start to roll into vortices, and for $\boldsymbol{z}_1$ and $\boldsymbol{z}_2$ diffusion modes more complex structures of the anisotropy high values in the whole wake flow. In figures 5 *(a)* and 5 *(b)*, respectively the vorticity norm and the divergence of the drift correction for the diffusion mode $\boldsymbol{z}_0$ is plotted. Like for the $Re = 300$ case, vorticity and divergence corrections are observed near the shear layers, outside and at the end of the recirculation zone, and just downstream in the launching area. Here again, high magnitudes of vorticity just downstream the maximum of anisotropy, are associated with the two pivotal regions of the shear layers rolling into vortices. Nevertheless, in the present HR LES case, results show some wiggles, which are here the footprint of insufficient convergence of the modes due to the low number of velocity snapshots available (see table 1). In that context the velocity induced by the neglected POD modes is less informative since the energy is less precisely spread over the modes.

We now consider the case LR DNS with sufficient velocity snapshots to get converged POD modes thus allowing us to analyse more precisely in three-dimensions the behaviour of the diffusion modes. Note however that due to the marginal resolution of LR DNS the flow yields a short recirculation zone length of the order $0.5D$, lower than the distance of $1.56D$ obtained with HR LES and expected for the Reynolds number $Re = 3900$ (Parnaudeau *et al.*, 2008). Figure 6 *(a-d)* is a mapping of three-dimensional iso-surfaces of the energy density for the diffusion modes $\boldsymbol{z}_0$, $\boldsymbol{z}_1$, $\boldsymbol{z}_2$, $\boldsymbol{z}_3$, and $\boldsymbol{z}_4$, in a cylinder wake flow at $Re = 3900$ (LR DNS). We observe that the diffusion mode $\boldsymbol{z}_0$ is one order of magnitude larger than the nonstationary modes. The flow turbulence exhibits hence a strong stationary behaviour. On the stationary diffusion mode $\boldsymbol{z}_0$ we see clearly the recirculation zone and the external delimitation of the cylinder wake as regions of higher and lower dissipation, respectively. The second and third nonstationary diffusion modes are related to structures with a characteristic length of the size of the Von Karman vortices. The fourth and fifth nonstationary diffusion modes correspond to much finer structures in the near cylinder wake. When compared with the case at $Re = 300$, the stationary diffusion mode $\boldsymbol{z}_0$ exhibits similar spatial distribution of

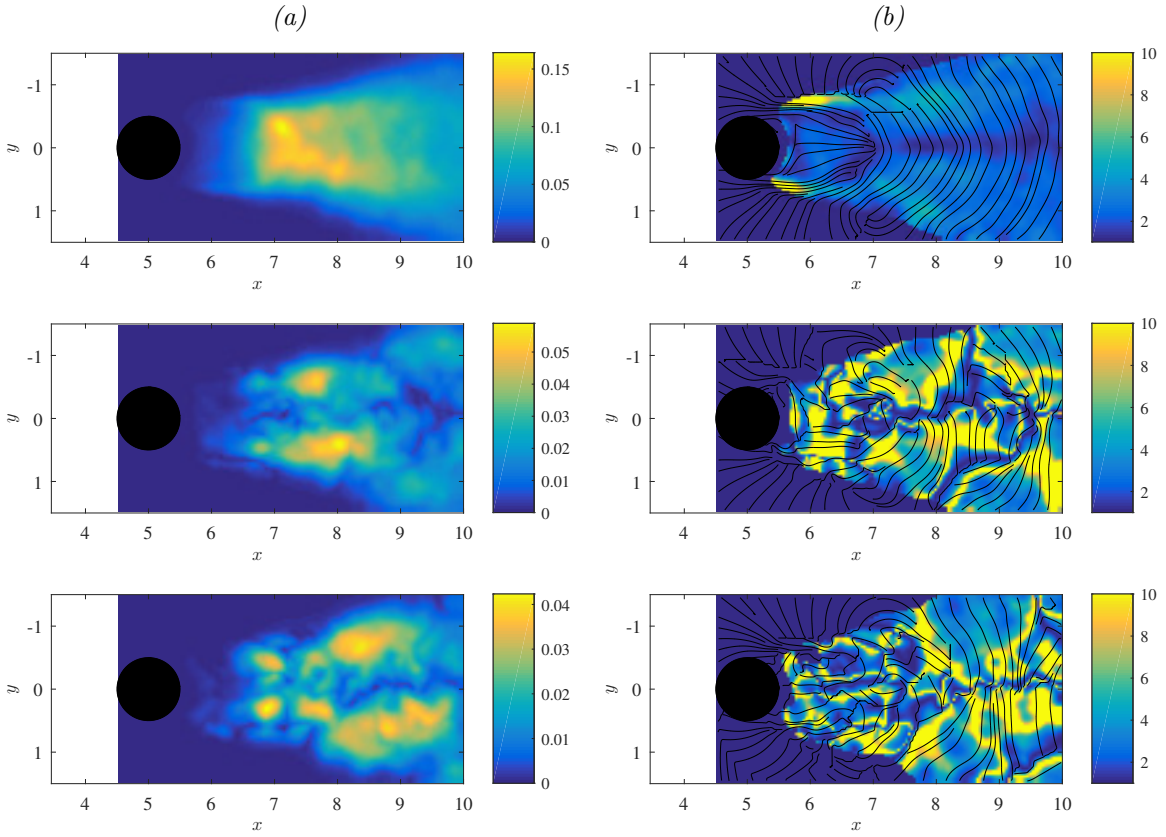

Figure 4: Local spectral representation of the matrix $\boldsymbol{a}$ in a cylinder wake flow at $Re = 3900$ (HR LES), for $n = 4$ POD modes: From top to bottom, diffusion modes $\boldsymbol{z}_0$, $\boldsymbol{z}_1$ and $\boldsymbol{z}_2$ respectively; *(a)*, Turbulent kinetic energy (square root of the sum of the squared eigenvalues); *(b)*, Small-scale anisotropy (ratio of the absolute value of the largest eigenvalue to the absolute value of the smallest eigenvalue). The streamlines represent the first proper diffusion direction (i.e. the eigenvectors corresponding to the largest eigenvalues of the small-scale variance tensor).

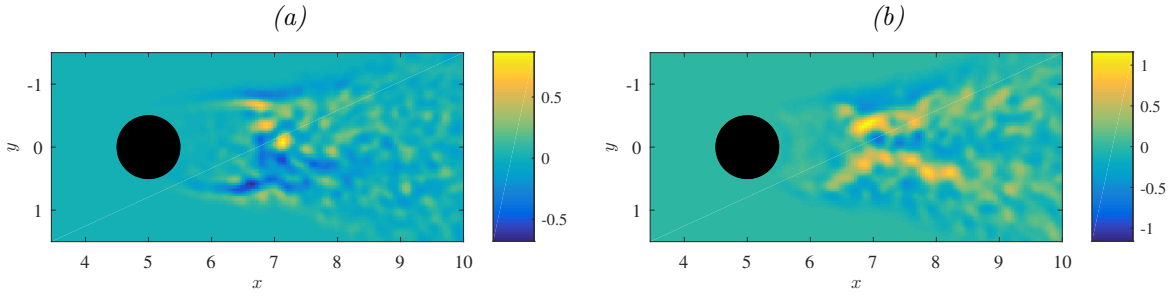

Figure 5: Spanwise vorticity component *(a)* and divergence *(b)* of the drift correction $-\frac{1}{2}\left(\boldsymbol{\nabla}\cdot\boldsymbol{a}\right)^T$ due to the diffusion mode $\boldsymbol{z}_0$, in a cylinder wake flow at $Re = 3900$ (HR LES) for $n = 4$ POD modes.

the small-scale turbulent kinetic energy, with the highest magnitudes reached at the end of the recirculation region and further downstream in the transitional zone with an arrow shape. Where the small-scale energy is high, the unresolved velocity and the diffusion are strong. The results we present next analyse the three-dimensionnal anisotropy of the diffusion modes.

In figures 7 *(a-c)* we plot the small-scale anisotropy isosurfaces of modes $\boldsymbol{z}_0$ and $\boldsymbol{z}_1$, respectively. No particular structure shows up on the nonstationary first modes (see e.g. anisotropy of mode $\boldsymbol{z}_1$ in figure 7 *b*). As a consequence, the anisotropic structures and consequently the diffusion geometry is principally described by the diffusion mode $\boldsymbol{z}_0$. Like for the two other cases, the diffusion mode $\boldsymbol{z}_0$ exhibits clearly, through local high magnitudes of the small-scale anisotropy, the two three-dimensional pivotal locations of the shear layers close to the cylinder just before station $x = 5.5$ at $y = \pm 0.5$ (figures 7 *a* and *c*). Downstream near station $x = 8 - 9$ in the middle of the transitional region where vortices detach from the cylinder and start to reorganise into the Karman vortex street, local high magnitudes of the anisotropy is indicated in figure 7 *(c)*. Farther downstream, near station $x \approx 12$ at the beginning of this pattern of regular and aligned vortices, the diffusion mode anisotropy is also maximum on the centreline.

In figure 8 *(a-e)* we plot vorticity and divergence iso-surfaces of the advection correction term for the three first diffusion modes. The stationary diffusion mode $\boldsymbol{z}_0$ unveils two large-scale effective contra-rotative vortices (figure 8 *a*). Like for the two other cases, the drift correction of the resolved (large-scale) velocity by the unresolved (small-scale) velocity is associated with high small-scale anisotropy and with vorticity corrections at the pivotal locations of the shear layers. Just behind the cylinder in the recirculation zone figure 8 *(b)* reveals a divergent area and two flat convergent zones near both shear layers. Thinner vorticity and diverging structures can be observed in the near cylinder wake on the nonstationary modes $\boldsymbol{z}_1$ and $\boldsymbol{z}_2$. The vorticity and divergence magnitudes involved in those modes are one order weaker than for the stationary diffusion mode. Downstream no significant structures are observed, indicating rather an homogeneous character of the small-scale velocity.

The diffusion modes analysis developed in the present paper identifies critical regions of the wake flow: the anisotropy exhibits mainly the pivotal location of the shear layers which are associated with large-scale vorticity corrections by the small-scale unresolved velocity and large-scale divergence corrections take also place in the vortex formation zone. For the wake flow considered, the results indicate that outside the recirculation area and the shear layer zones an eddy viscosity assumption is likely valid. However in the near wake, such an assumption is too strong and corrective advection effects as well as structured energy dissipation effects must be taken into account. These findings support the recent results of Chandramouli *et al.* (2016) who demonstrated the good contributions of such novel stochastic small-scale modelling in the context of coarse-grid large eddy simulation of a wake flow.

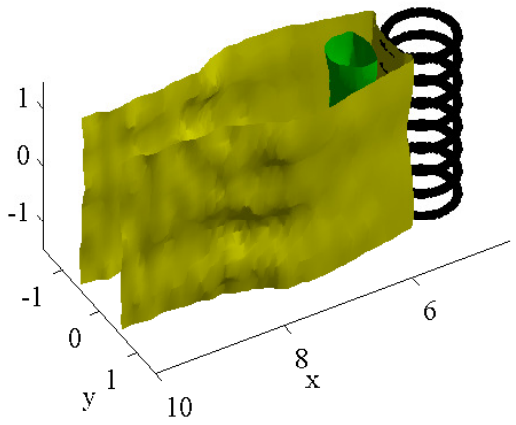

(a) $\sqrt{\lambda_0}tr(\boldsymbol{z}_0) = (0.25; 0.75)$

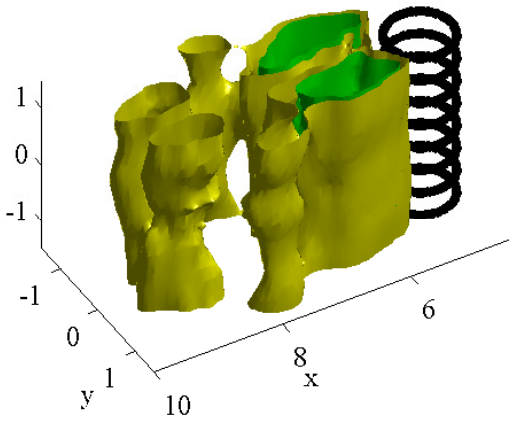

(b) $\sqrt{\lambda_1}tr(\boldsymbol{z}_1) = (0.02; 0.0125)$

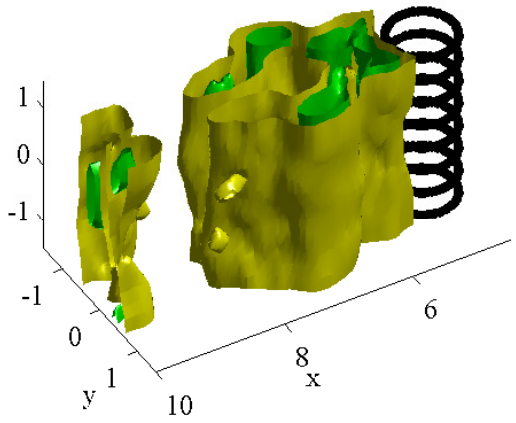

(c) $\sqrt{\lambda_2}tr(\boldsymbol{z}_2) = (0.02; 0.0125)$

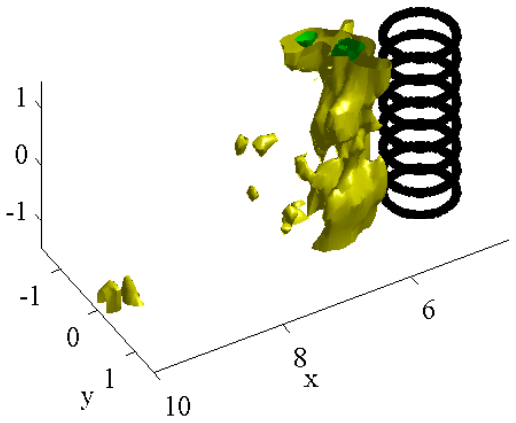

(d) $\sqrt{\lambda_3}tr(\boldsymbol{z}_3) = (0.012; 0.009)$

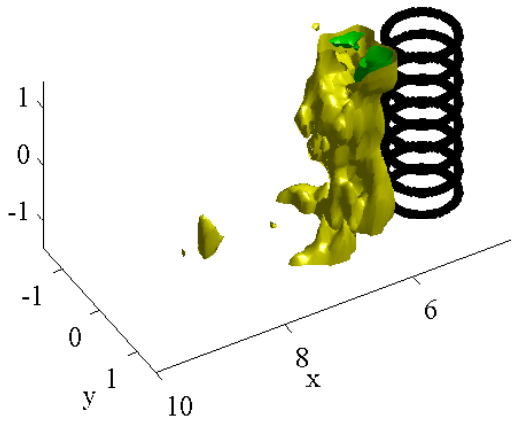

(e) $\sqrt{\lambda_4}tr(\boldsymbol{z}_4) = (0.012; 0.009)$

Figure 6: Local spectral representation of the matrix $\boldsymbol{a}$ in a cylinder wake flow at $Re = 3900$ (LR DNS), for $n = 4$ POD modes: *(a-e)*, Small-scale turbulent kinetic energy isosurfaces of the diffusion modes $\boldsymbol{z}_0$ to $\boldsymbol{z}_4$, respectively. At places where the energy is high, the unresolved velocity and the diffusion are strong. The green isosurfaces are associated with higher values than the yellow isosurfaces.

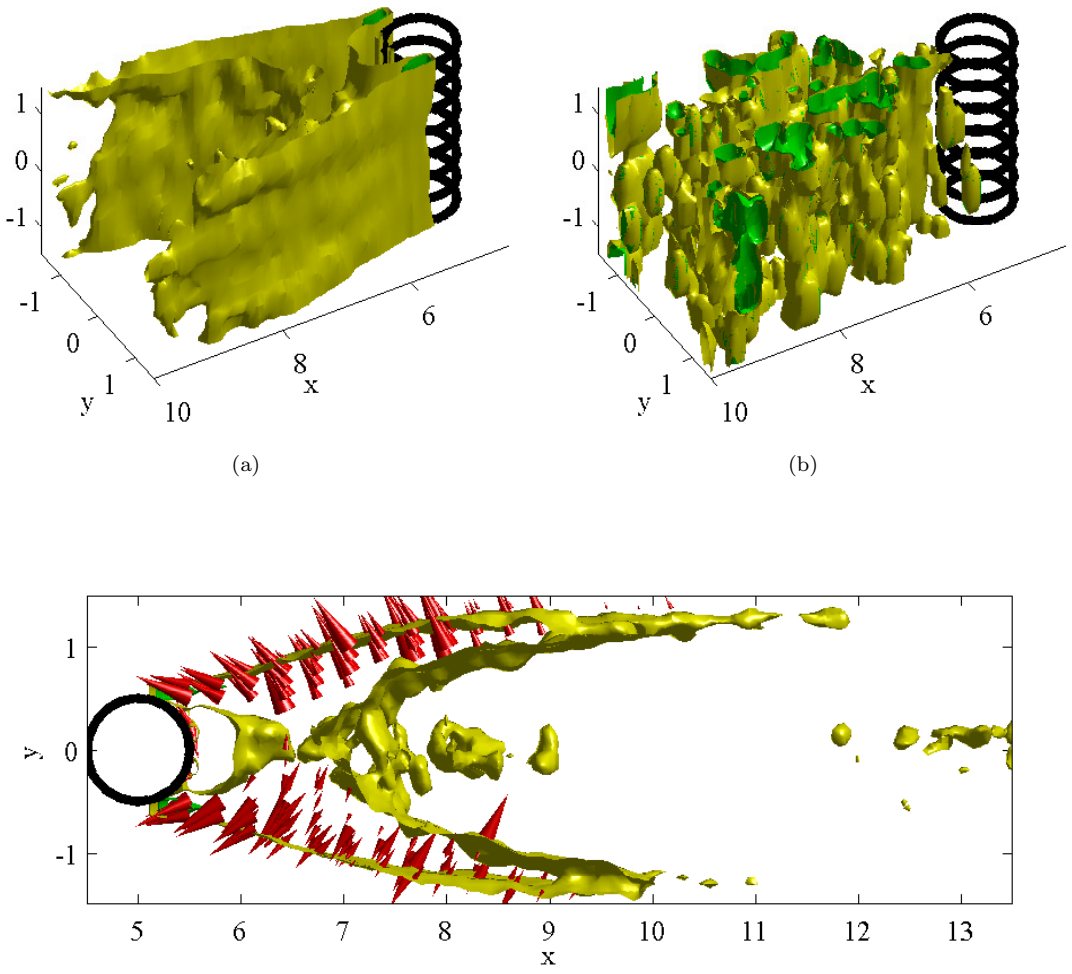

Figure 7: Local spectral representation of the matrix $\boldsymbol{a}$ in a cylinder wake flow at $Re = 3900$ (LR DNS), for $n = 4$ POD modes: *(a,b)*, Small-scale anisotropy isosurfaces of modes $\boldsymbol{z}_0$ and $\boldsymbol{z}_1$, respectively; *(c)*, Top view of small-scale anisotropy isosurface of modes $\boldsymbol{z}_0$. The red cones represent the preferential diffusion directions (i.e. the eigenvectors corresponding to the largest eigenvalues of the small-scale variance tensor). The green surface ($\sigma = 6$) is associated with a higher anisotropy of both the small-scale velocity and the diffusion, than the yellow surface ($\sigma = 3$).

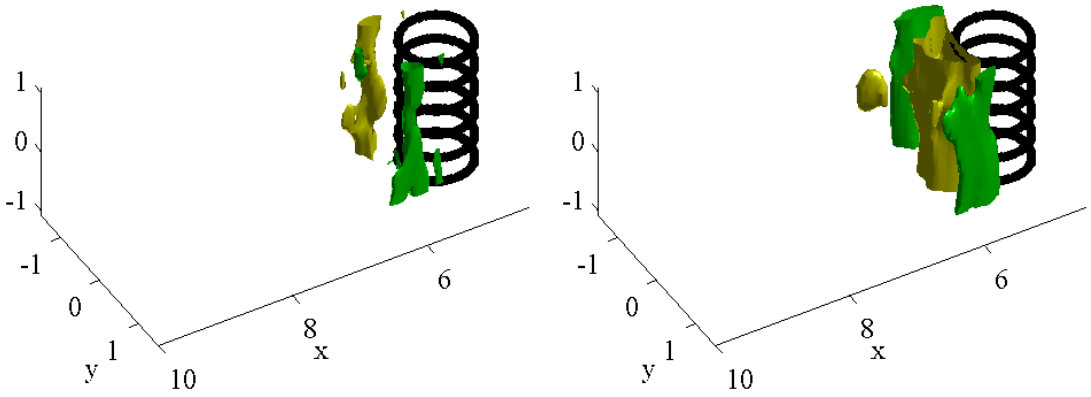

(a) $\frac{1}{2}|\boldsymbol{\nabla} \times (\boldsymbol{\nabla} \cdot \boldsymbol{z}_0)^T| = 0.7$

(b) $\frac{1}{2}|\boldsymbol{\nabla} \cdot (\boldsymbol{\nabla} \cdot \boldsymbol{z}_0)^T| = 0.4$

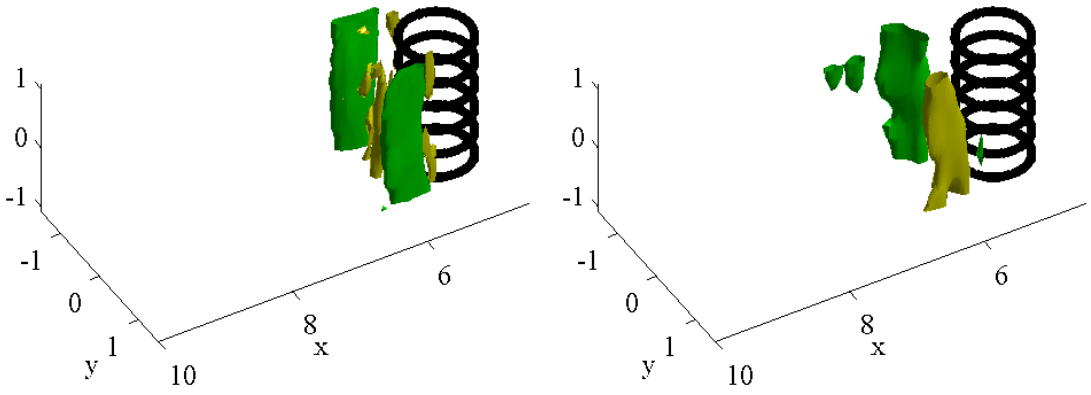

(c) $\frac{1}{2}|\boldsymbol{\nabla} \times (\boldsymbol{\nabla} \cdot \boldsymbol{z}_1)^T| = 0.07$

(d) $\frac{1}{2}|\boldsymbol{\nabla} \cdot (\boldsymbol{\nabla} \cdot \boldsymbol{z}_1)^T| = 0.06$

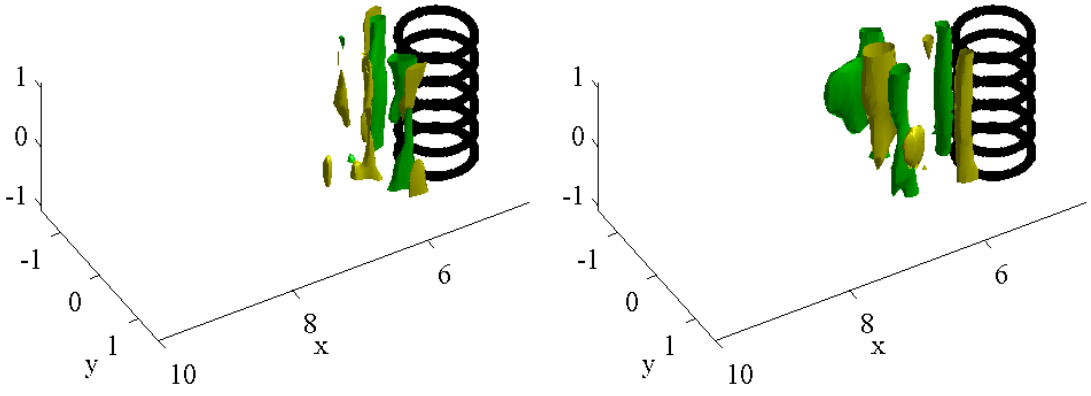

(e) $\frac{1}{2}|\boldsymbol{\nabla} \times (\boldsymbol{\nabla} \cdot \boldsymbol{z}_2)^T| = 0.07$

(f) $\frac{1}{2}|\boldsymbol{\nabla} \cdot (\boldsymbol{\nabla} \cdot \boldsymbol{z}_2)^T| = 0.06$

Figure 8: Vorticity *(Left)* and divergence *(Right)* isosurfaces of the drift correction $-\frac{1}{2}(\boldsymbol{\nabla} \cdot \boldsymbol{a})^T$ in a cylinder wake flow at $Re = 300$, for $n = 4$ POD modes: *(a,b)*, Diffusion mode $\boldsymbol{z}_0$; *(c,d)*, Diffusion mode $\boldsymbol{z}_1$; *(e,f)*, Diffusion mode $\boldsymbol{z}_2$. On the left column, the green iso-surfaces are associated with a vorticity vector aligned downward whereas the yellow iso-surfaces are associated with a vorticity vector aligned upward. On the right column the green surfaces stand for areas with iso-negative divergence (convergent zone) whereas the yellow iso-surfaces correspond to a positive divergence (divergent zone).

5.3 Chronos reconstruction

In this section we aim at assessing the performance of the subgrid term introduced by the stochastic representation of the small-scales. We compare the *chronos* trajectories that were directly reconstructed from the reduced-order dynamical system (3.4.3) to the observed *chronos*. Let us note that almost long time perfect trajectories could be recovered through data assimilation strategies (D'Adamo *et al.*, 2007; Artana *et al.*, 2012; Cordier *et al.*, 2013; Protas *et al.*, 2015). However with such techniques it would be difficult to identify the intrinsic role of the subgrid scheme compared to a least-squares adaption of all the dynamics coefficients along the whole sequence. We therefore prefer to rely on a direct reconstruction strategy in which no identification, like least-squares or data-assimilation estimation procedures of the dynamical coefficients, is introduced. Note that such a direct reconstruction requires an additional stabilization, like a closure model, to ensure the long-term boundedness of the solution. In our model, the stabilization is inherited from the rigorously derived subgrid terms based on the variance of the unresolved velocity component. In the following, we compare temporal reconstructions obtained with our stochastic Galerkin model to those provided by different deterministic POD models.

The results presented so far on the diffusion mode analysis did not necessitate any knowledge of the Reynolds number to compute both the diffusion and the drift correction of the large-scale by the unresolved small-scale. The assessments have been conducted in particular with the LR DNS data for which the flow does not fit with the theoretical wake flow at Reynolds number $Re = 3900$. We now turn to reduced-order dynamical systems which, in contrast, need for their evaluation flow data sets that are physically consistent with the Reynolds number considered. Hence in the following we consider the DNS case at Reynolds number $Re = 300$ and the HR LES case at Reynolds number $Re = 3900$.

The modes mean energy, λ_i, and the *topos*, ϕ_i, are computed from the whole sequence of snapshots ($N = 3999$ for $Re = 300$ and $N = 251$ for $Re = 3900$). As for the initial condition, we used the referenced values of the *chronos*, denoted b_i^{ref}, computed directly from the snapshots covariance diagonalization. Then, regarding the *chronos* spectra, an optimal time sub-sampling is chosen, as explained in §3.3. Afterward, using the residual velocity and the *chronos*, the variance tensor, a, is estimated. The coefficients of the reduced-order dynamical system of *chronos* (3.4.3) are directly computed using discrete derivation schemes. The *chronos* trajectories are simulated with a 4-th order Runge-Kutta integration method, with $b^{ref}(t = 0)$ as initial condition.

Figures 9 and 10 show examples of the reconstruction of the *chronos* for $n = 2$ at Reynolds number $Re = 300$ and $n = 10$ at Reynolds number $Re = 3900$, respectively, for the classical POD method (blue plot) and for the proposed modelling with respectively a stationary and a nonstationary variance tensor defined on the subspace associated with the *chronos* basis (red plot). At Reynolds number $Re = 300$, the first two modes carry most of the energy. The reference b_i^{ref} (black plot) are superimposed for comparison purposes. It can be observed that our stochastic model follows the references quite well whereas the deterministic model blows up. Let us point out that here both reduced models are completely parameter free. No constant has been tuned to adapt any viscosity model. Figures 11 and 12 describe the error evolution along time. Approximating the square of the actual unresolved *chronos* by the time average of their squares, we defined the error as follows:

$$\begin{aligned} err(t) &= T\frac{\left\|u^{ref}-u\right\|_{L^2(\Omega)}}{\|u^{ref}\|_{L^2(\Omega\times[0,T])}}, \\ &= T\frac{\left\|\sum_{i=1}^{n}\left(b_i^{ref}-b_i\right)\phi_i+\sum_{i=n+1}^{N}b_i^{ref}\phi_i\right\|_{L^2(\Omega)}}{\left\|\sum_{i=0}^{N}b_i^{ref}\phi_i\right\|_{L^2(\Omega\times[0,T])}}, \\ &\approx \left(\frac{\sum_{i=1}^{n}\left(b_i^{ref}-b_i\right)^2+\sum_{i=n+1}^{N}\lambda_i}{\|\phi_0\|^2_{L^2(\Omega)}+\sum_{i=1}^{N}\lambda_i}\right)^{1/2}, \end{aligned} \tag{5.3.1}$$

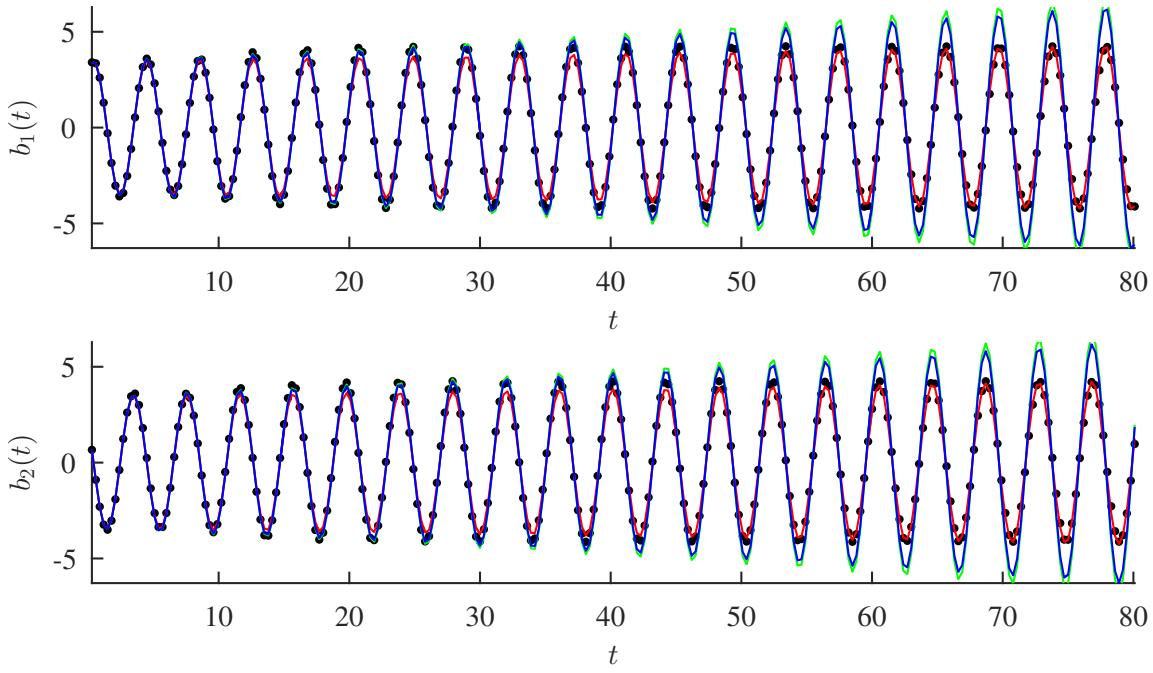

Figure 9: Reconstruction of the two first *chronos* for a wake flow at Reynolds number $Re = 300$, with $n = 2$ POD modes and with a stationary variance tensor: (black dots), observed references; (blue line), standard POD-Galerkin; (red line), proposed the stochastic representation; (green line), modal eddy viscosity reduced-order model. The initial condition, at $t = 0$, is identical for all methods.

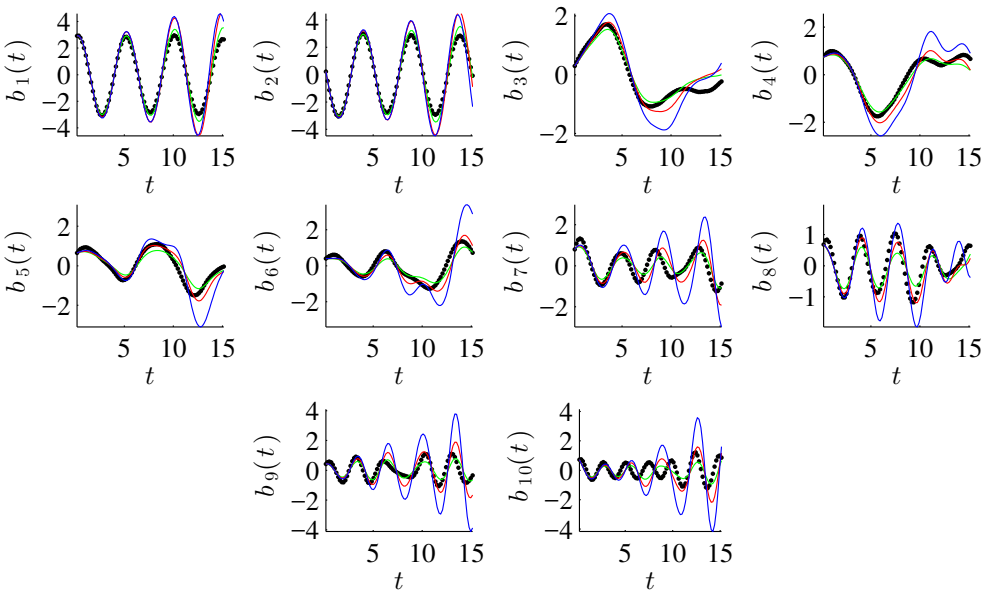

Figure 10: Reconstruction of the ten first *chronos* for a wake flow at Reynolds number $Re = 3900$ (HR LES), with $n = 10$ POD modes and with a variance tensor expressed as a linear function of the *chronos*: (black dots), observed references; (blue line), standard POD-Galerkin; (red line), proposed the stochastic representation; (green line), modal eddy viscosity reduced-order model. The initial condition, at $t = 0$, is identical for all methods.

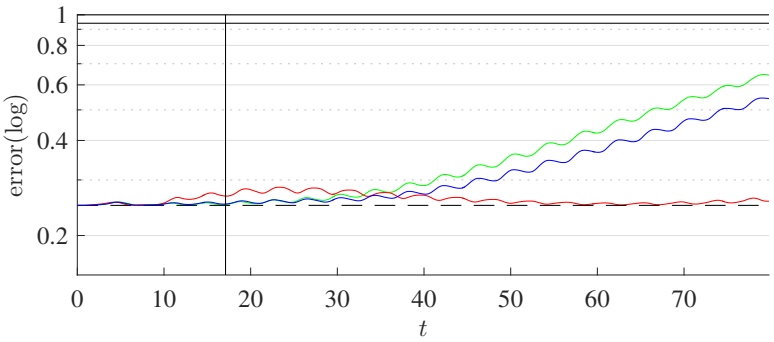

Figure 11: Normalized reconstruction error for a wake flow at Reynolds number $Re = 300$, with $n = 2$ POD modes: (blue line), standard POD Galerkin (without eddy viscosity); (red line), proposed model with a stationary variance tensor; (green line), modal eddy viscosity reduced-order model. The modal eddy viscosity coefficients are estimated on the three first vortex shedding. The end of the learning period is indicated by a vertical bar at $t = 18$. The dashed line indicates the error associated with the mode truncation : $\sum_{i=n+1}^{N} \lambda_i$. The black solid line is the error when we only consider the temporal mean velocity.

which is greater than the minimal error associated to the modal truncation:

$$err(t) \quad \geqslant \quad \left(\frac{\sum_{i=n+1}^{N} \lambda_i}{\|\phi_0\|^2_{L^2(\Omega)} + \sum_{i=1}^{N} \lambda_i} \right)^{1/2}. \tag{5.3.2}$$

Equation (5.3.1) defines the criterion error plotted in figures 11 and 12, whereas (5.3.2) constitutes a lower bound of this error. In figures 11 and 12, we displayed successively the error plots obtained for the standard POD Galerkin model without subgrid dissipative term, for our model with stationary and nonstationary variance tensors, and finally for a deterministic modal eddy viscosity model. This subgrid model, proposed in Rempfer & Fasel (1994) consists in modifying the reduced-order system by adding a strong isotropic diffusive term (Laplacian) to stabilize the system. This eddy viscosity is said to be modal since different viscosity coefficients are attached to each *chronos*. Those coefficients are estimated by a least squares fitting on the first quarter of the data. Modal eddy viscosity in its least squares form ressembles indeed to a data assimilation strategy in which the best stationary isotropic dissipative forcing is estimated from the discrepancy between the model and the data. The same isotropic dissipation is imposed on the whole fluid domain at every time step. As such this subgrid dissipation is much more difficult to interpret in terms of local signatures of the small-scale coherent structures.

In figures 11 and 12, the dashed lines indicate the minimal error associated with the reduced subspace truncation error. The black solid line corresponds to the error level associated with the temporal mean velocity – i.e. setting all the *chronos* to 0. In this case:

$$err_{|b=0}(t) \quad \approx \quad \left(\frac{\sum_{i=1}^{N} \lambda_i}{\|\phi_0\|^2_{L^2(\Omega)} + \sum_{i=1}^{N} \lambda_i} \right)^{1/2}.$$

This term does not constitute an upper bound of the error. However, it provides the error level reached by the null model. In figures 11 and 12, fixing a log-scale for the y axis, we readily observe the exponential divergence of the standard POD reduced-order model (in blue).

We observe that at Reynolds number $Re = 300$ the modal eddy viscosity model does not capture accurately, on a long time period, the complex non-linear dynamics undergone by the non-resolved modes (figure 11). Just after the learning period (3 vortex shedding), the eddy viscosity models performs well. However, they start diverging after 30 time steps. The stationary model leads, in contrast, to a stable simulation in the long run.

For the case HR LES at Reynolds number $Re = 3900$ (figure 12), we compared the eddy viscosity approaches (modal and constant) with stationary and nonstationary models of the variance tensors. In this case the variance tensor as well as the eddy viscosity coefficients have been estimated on 3 vortex shedding as well. The performances of the modal and single characteristic times attached to the variance tensor have been evaluated and compared. The error plots are shown in figure 12. The introduction of different small-scale characteristic time steps associated with the different modes significantly improves the results that were obtained for a single common characteristic time. Both approaches are equivalent for short time period only. The introduction of modal characteristic times is clearly beneficial in the long run. The nonstationary representation performs only slightly better than the stationary one for this wake flow. However, the piece of information brought by the nonstationary diffusion modes enables meaningful analysis of the small-scale contribution (see §5.2). Both eddy viscosity approaches perform well either in their modal or constant versions. Modal eddy viscosity appears to work better when a small number of modes is involved. The (stationary or nonstationary) variance tensor models that are associated with modal characteristic time scales exhibit nearly the same stabilizing skills as the eddy viscosity models. Both models lead to similar error levels. Nevertheless, it must be outlined that the two approaches are based on different assumptions. Eddy viscosity relies intrinsically on an homogeneous isotropic diffusion with no preferential direction of energy dissipation. The diffusion remains constant whatever the considered region: in the near or far wake regions, and even in the shear layers. However, as a fixed constant estimated through a mean squares procedure, it provides the optimal amount of missing energy dissipation (with respect to a spatio-temporal mean of the squared norm) that is required to stabilize the reduced dynamical system. Conversely, as shown in the previous section, the variance tensor and the associated diffusion modes provide a finer representation of the small-scales action in terms of energy dissipation but also in terms of energy redistribution. As for the simulation of the reduced system, both models lead to comparable error levels. They bring stability to the system in a similar way, but the variance tensor models unveil important hints on the small-scale flow structuration.

6 Conclusion

We investigated the study of reduced-order modelling based on a stochastic representation of the small-scales proposed by Mémin (2014) and Resseguier *et al.* (2017*a*). This principle gives rise naturally to a drift correction generated by the inhomogeneity of the small-scale velocity variance and to an inhomogeneous diffusion term. The diffusion term is closely related to eddy viscosity assumption. Indeed, for an isotropic divergence-free random field, the stochastic representation boils down to the classical eddy viscosity assumption. A POD Galerkin projection of the corresponding stochastic Navier-Stokes equations provides a modified reduced-order dynamical system that includes a linear term gathering the effects of the effective advection and of the diffusion exerted by the unresolved small-scale component. This function directly depends on the small-scale variance that must be specified to close the system.

We proposed in this study a modelling based on the decomposition of this variance tensor on the *chronos* basis. The estimation has been performed on the residuals between the snapshots measurements and their resolved reconstruction on the *topos* basis. The coefficients of this decomposition quoted as the *diffusion modes* constitute meaningful features for the interpretation of the small-scale statistical organization. They allow us to examine in details the principal directions of the small-scale energy dissipation and also to extract advective structures generated by the small-scale velocity.

The diffusion modes analysis has been applied to a circular cylinder wake flow. For this flow configurations in the laminar and in the subcritical regimes, the anisotropy of the diffusion modes determine

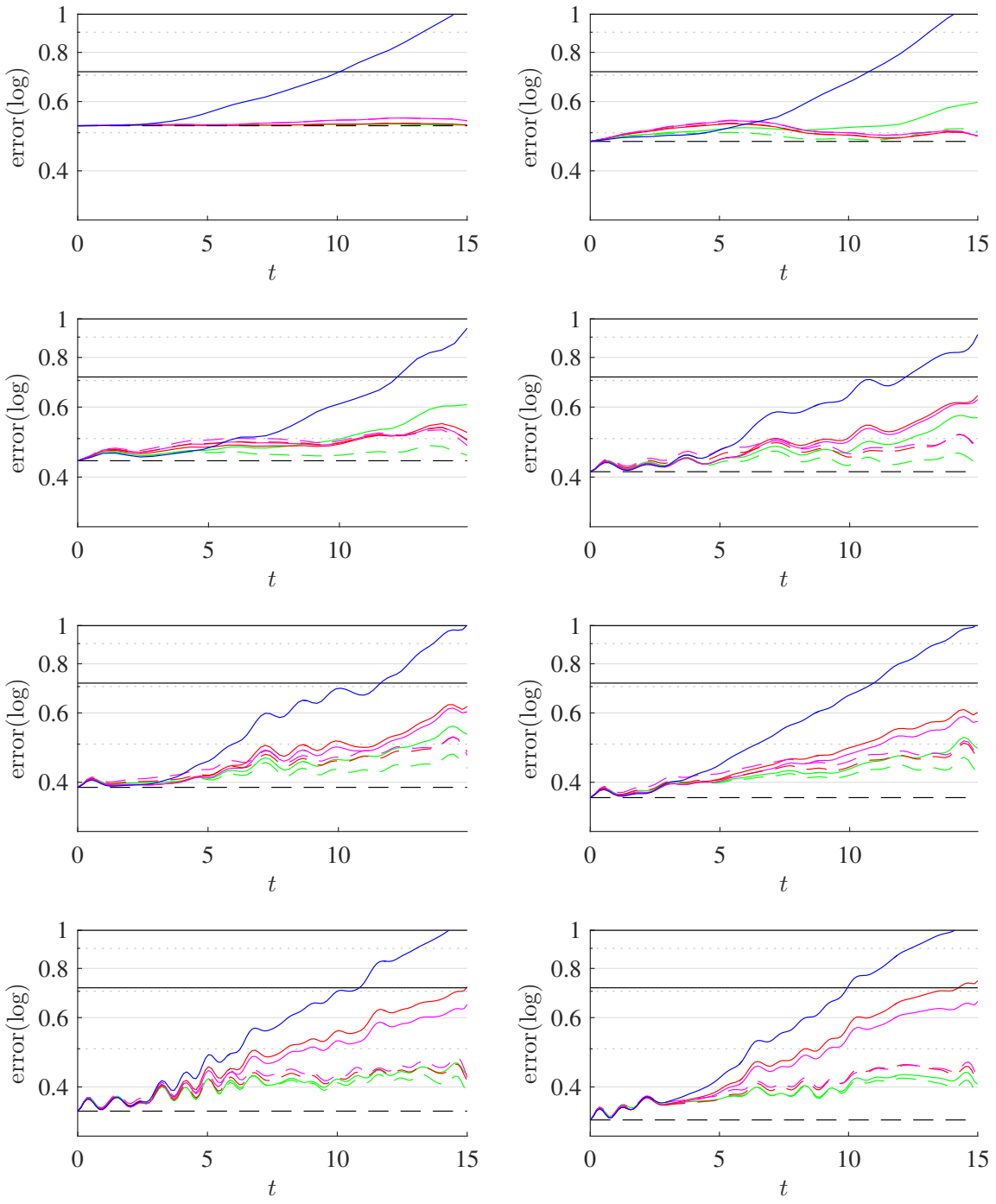

Figure 12: Normalized reconstruction error for a wake flow at Reynolds number $Re = 3900$ (HR LES), with $n = 2$, 4, 6, 8, 10, 12, 14 and 16 POD modes: (blue line), standard POD Galerkin without eddy viscosity; (red/magenta line), proposed model with a stationary/nonstationary variance tensor, solid and dashed line with single and modal characteristic time, respectively; (green line), solid and dashed with eddy viscosity and modal eddy viscosity reduced-order model, respectively. The eddy viscosity coefficients are estimated through a least squares fit on the whole data sequence. The variance tensors are also estimated from a temporal mean on the whole sequence. The dashed line indicates the error associated with the mode truncation : $\sum_{i=n+1}^{N} \lambda_i$. The black solid line is the error when we only consider the temporal mean velocity.

regions of the flow that are key players. The largest magnitudes of the anisotropy zero-mode (stationary mode) occur in the vicinity of the pivotal zone of the shear layers rolling into vortices and where the drift correction is effective.

Finally, the diffusion modes were coupled with modal characteristic time scales to provide a subgrid model. For wake flows, stabilizing skill are comparable to that obtained with optimally identified isotropic eddy viscosity models. Such a stochastic approach consisting of a rigorously derived subgrid term, may easily be applied to other turbulent flow configurations, for instance boundary layer flows that are known to develop complex multi-scale mechanisms. Moreover, it will be interesting to see whether our proposed stochastic POD models could be used to design novel physics-based subgrid scale models for LES approaches.

Other extensions of this methodology include online quantification of model errors for ensemble data assimilation procedures. The authors are already pursuing this work in the context of reduced order models but also in geophysical fluid dynamics (Resseguier *et al.*, 2017*a*,*b*).

Acknowledgements

The authors acknowledge the support of the SEACS project funded by the Brittany clusters of excellence (Cominslab, Lebesgue, and Mer). The authors thank Johan Carlier for providing the data case LR DNS.

References

Andrews, D. & McIntyre, M. 1976 Planetary waves in horizontal and vertical shear: the generalized Eliassen- Palm relation and the zonal mean acceleration. *J. Atmos. Sci.* **33**, 2031–2048.

Artana, G., Cammilleri, A., Carlier, J. & Mémin, E. 2012 Strong and weak constraint variational assimilations for reduced order fluid flow modeling. *J. Comp. Phys* **231** (8), 3264–3288.

Aspden, A., Nikiforakis, N., Dalziel, S. & Bell, J.B. 2008 Analysis of implicit LES methods. *App. Math. Comp. Sci.* **3** (1), 103–126.

Aubry, N., Holmes, P., Lumley, J.L. & Stone, E. 1988 The dynamics of coherent structures in the wall region of a turbulent boundary layer. *J. Fluid Mech.* **192**, 115–173.

Bardina, J., Ferziger, J.H. & Reynolds, W.C. 1980 Improved subgrid scale models for large eddy simulation. In *13th Fluid Mechanics & Plasma Dynamics Conference* (ed. AIAA), , vol. 80, p. 1380.

Boris, J.P., Grinstein, F.F., Oran, E.S. & Kolbe, R.L. 1992 New insights into large-eddy simulation. *Fluid Dynamics Research* **10**, 199–228.

Boussinesq, J. 1877 Essai sur la théorie des eaux courantes. Mémoires présentés par divers savants à l'Académie des Sciences, 23 (1): 1–680.

Brooke, M., Kontomaris, K., Hanratty, T. & McLaughlin., J. 1992 Turbulent deposition and trapping of aerosols at a wall. *Phys. FLuids* pp. 825–834.

Cammilleri, A., Gueniat, F., Carlier, J., Pastur, L., Mémin, E., Lusseyran, F. & Artana., G. 2013 POD-spectral decomposition for fluid flow analysis and model reduction. *Theor. and Comp. Fluid Dyn.* Accepted for publication.

Caporaloni, M., Tampieri, F., Trombetti, F. & Vittori, O. 1975 Transfer of particles in non- isotropic air turbulence. *J. Atmos. Sci.* **32**, 565–568.

Cazemier, W., Verstappen, R. & Veldman, A. 1998 Proper orthogonal decomposition and low-dimensional models for driven cavity flows. *Phys. Fluids* **10** (7), 1685–1699.

Chandramouli, P., Heitz, D., Laizet, S. & Mémin, E. 2016 Coarse-grid large eddy simulations in a wake flow with new stochastic small-scale models. ArXiv report.

Cordier, L., Noack, B.R., Tissot, G., Lehnasch, G., Delville, J., Balajewicz, M., Daviller, G. & Niven, R.K. 2013 Identification strategies for model-based control. *Exp. Fluids* **54** (8), 1–21.

D'Adamo, J., Papadakis, N., Mémin, E. & Artana, G. 2007 Variational assimilation of POD low-order dynamical systems. *J. of Turb.* **8** (9), 1–22.

Deane, A., Kevrekidis, I., Karniadakis, G. & Orszag, S. 1991 Low-dimensional models for complex geometry fows: Application to grooved channels and circular cylinders. *Phys. Fluids* **3** (10), 2337.

Galetti, B., Botaro, A., Bruneau, C.-H. & Iollo, A. 2007 Accurate model reduction of transient and forced wakes. *Eur. j. Mech. B, Fluids* **26** (3), 354–366.

Genon-Catalot, V., Laredo, C. & Picard, D. 1992 Non-parametric estimation of the diffusion coefficient by wavelets methods. *Scandinavian Journal of Statistics* pp. 317–335.

Gent, P., Willebrand, J., McDougall, T. & McWilliams, J. 1995 Parameterising eddy-induced tracer transports in ocean circulation models. *J. Phys. Oceanogr.* **25**, 463–474.

Haworth, D. & Pope, S. 1986 A generalized langevin model for turbulent flows. *Phys. Fluids* **29**, 387–405.

Holmes, P., Lumley, J.L. & Berkooz, G. 1996 *Turbulence, coherence structures, dynamical systems and symetry*. Cambridge university press.

Kalb, V. & Deane, A. 2007 An intrinsic stabilization scheme for proper orthogonal decomposition based low-dimensional models. *Phys. Fluids* **19** (5).

Karamanos, G. & Karniadakis, G. 2000 A spectral vanishing viscosity method for large-eddy simulations. *J. Comp. Phys.* **163** (1), 22–50.

Koopman, B. 1931 Hamiltonian systems and transformations in Hilbert space. *Proc. Natl. Acad. Sci.* .

Kraichnan, R. 1987 Eddy viscosity and diffusivity: exact formulas and approximations. *Complex Systems* **1** (4-6), 805–820.

Laizet, S. & Lamballais, E. 2009 High-order compact schemes for incompressible flows: a simple and efficient method with the quasi-spectral accuracy. *J. Comp. Phys.* **228** (15), 5989–6015.

Laizet, S. & Li, N. 2011 Incompact3d: A powerful tool to tackle turbulence problems with up to $0(10^5)$ computational cores. *International Journal for Numerical Methods in Fluids* **67** (11), 1735–1757.

Lamballais, E., Fortuné, V. & Laizet., S. 2011 Straightforward high-order numerical dissipation via the viscous term for direct and large eddy simulation. *J. Comp. Phys.* **230**, 3270–3275.

Lilly, D. 1992 A proposed modification of the Germano subgrid-scale closure. *Phys. Fluids* **3**, 2746–2757.

Ma, X., Karamanos, G.-S. & Karniadakis, G.E. 2000 Dynamics and low-dimensionality of a turbulent near wake. *J. Fluid Mech.* **410**, 29–65.

Ma, X., Karniadakis, G.E., Park, H. & Gharib, M. 2002 DPIV-driven simulation: a new computational paradigm. *Proc. R. Soc. Lond. A* **459**, 547–565.

Macinnes, J. & Bracco, F. 1992 Stochastic particles dispersion modelling and the tracer-particle limi. *Phys. Fluids* **4** (12), 2809–2824.

Mémin, E. 2014 Fluid flow dynamics under location uncertainty. *Geophysical & Astrophysical Fluid Dynamics* **108** (2), 119–146.

Métais, O. & Lesieur, M. 1992 Spectral large-eddy simulation of isotropic and stably stratified turbulence. *J. Fluid Mech.* **239**, 157.

Mezic, I. 2005 Spectral properties of dynamical systems, model reduction and decompositions. *Nonlinear Dyn* **41** (1-3), 309–325.

Noack, B., Morzynski, M. & Tadmor, G. 2010 *Reduced-Order Modelling for Flow Control*, *CISM Courses and Lectures*, vol. 528. Springer-Verlag.

Noack, B., Papas, P. & Monkevitz, P.A. 2005 The need for a pressure-term representation in empirical Galerkin models of incompressible shear flows. *J. Fluid Mech.* **523**, 339–365.

Östh, J., Noack, B., Krajnović, S., Barros, D. & Borée, J. 2014 On the need for a nonlinear subscale turbulence term in POD models as exemplified for a high-reynolds-number flow over an ahmed body. *J. Fluid Mech.* **747**, 518–544.

Parnaudeau, P., Carlier, J., Heitz, D. & Lamballais, E. 2008 Experimental and numerical studies of the flow over a circular cylinder at reynolds number 3900. *Phys. Fluids* **20** (8), 085101.

Parnaudeau, P., Lamballais, E., Heitz, D. & Silvestrini, J.H. 2004 Combination of the immersed boundary method with compact schemes for DNS of flows in complex geometry. In *Direct and Large-Eddy Simulation V*, pp. 581–590. Springer.

Pasquetti, R. 2006 Spectral vanishing viscosity method for large-eddy simulation of turbulent flows. *J. Sci. Comp.* **27** (1-3), 365–375.

Piomelli, U., Cabot, W.H., Moin, P. & Lee, S. 1991 Subgrid scale backscatter in turbulent and transitional flows. *Phys. Fluids* **3** (7), 1766–1771.

Pope, S. 1994 Lagrangian pdf methods for turbulent flows. *Annu. Rev. Fluid Mech.* .

Pope, S. 2000 *Turbulent flows*. Cambridge University Press.

Protas, B., Noack, B. R & Östh, J. 2015 Optimal nonlinear eddy viscosity in Galerkin models of turbulent flows. *J. Fluid Mech.* **766**, 337–367.

Reeks, M. 1983 The transport of discrete particles in inhomogeneous turbulence. *J. Aerosol Sci.* **14** (6), 729–739.

Rempfer, D. & Fasel, H.F. 1994 Evolution of three-dimensional coherent structures in a flat-plate boundary layer. *J. Fluid Mech.* **260**, 351–375.

Resseguier, V., Mémin, E. & Chapron, B. 2017*a* Geophysical flows under location uncertainty, part I: Random transport and general models. In revision for Geophysical & Astrophysical Fluid Dynamics.

Resseguier, V., Mémin, E. & Chapron, B. 2017*b* Geophysical flows under location uncertainty, part II: Quasi-geostrophic models and efficient ensemble spreading. In revision for Geophysical & Astrophysical Fluid Dynamics.

Resseguier, V., Mémin, E. & Chapron, B. 2017*c* Geophysical flows under location uncertainty, part III: SQG and frontal dynamics under strong turbulence. In revision for Geophysical & Astrophysical Fluid Dynamics.

Rowley, C., Mezić, I., Bagheri, S., Schlatter, P. & Henningson, D. 2009 Spectral analysis of nonlinear flows. *J. Fluid Mech.* **641**, 115–127.

Sawford., B. 1986 Generalized random forcing in random-walk models of turbulent dispersion model. *Phys. Fluids* **29**, 3582–3585.

Schmid, P. 2010 Dynamic mode decomposition of numerical and experimental data. *J. Fluid Mech.* **656**, 5–28.

Sehmel, G. 1970 Particle deposition from turbulent air flow. *J. Geophys. Res.* **75**, 1766–1781.

Semaan, R., Kumar, P., Burnazzi, M., Tissot, G., Cordier, L. & Noack, B. R. 2016 Reduced-order modeling of the flow around a high-lift configuration with unsteady coanda blowing. *J. Fluid Mech.* **800**, 72–110.

Sirovich, L. 1987 Turbulence and the dynamics of coherent structures. *Quart. J. Applied Math.* **45**, 561–590.

Smagorinsky, J. 1963 General circulation experiments with the primitive equation: I. the basic experiment. *Month. Weath. Rev.* **91**, 99–165.

Tadmor, E. 1989 Convergence of spectral methods for nonlinear conservation laws. *SIAM J. Numer. Anal* **26** (1), 30–44.

Takens, F. 1981 Detecting strange attractors in turbulence. In *Dynamical Systems and Turbulence*, *Lecture Notes in Mathematics*, vol. 898, pp. 366–381. Springer-Verlag.